HEMP STEM-DERIVED ACTIVATED CARBON PRODUCTION AND PERFORMANCE ANALYSIS FOR SUPERCAPACITOR APPLICATIONS

A Thesis Submitted to
the Graduate School of Engineering and Sciences of
İzmir Institute of Technology
in Partial Fulfillment of the Requirements for the Degree of

MASTER OF SCIENCE

in Energy Engineering

by
ECE İNAN

July 2025

İZMİR

We approve the thesis of **Ece İNAN**

Examining Committee Members:

Assoc. Prof. Dr. Başar ÇAĞLAR

Department of Energy Systems Engineering, İzmir Institute of Technology

---

Prof. Dr. Özgenç EBİL

Department of Chemical Engineering, İzmir Institute of Technology

---

Assoc. Prof. Dr. Yavuz GÖKÇE

Department of Chemical Engineering, Ankara University

11 July 2025

Assoc. Prof. Dr. Başar ÇAĞLAR
Supervisor, Department of Energy Systems Engineering, İzmir Institute of Technology

---

Prof. Dr. Selahattin YILMAZ
Co-Supervisor, Department of Chemical Engineering, İzmir Institute of Technology

---

Prof. Dr. Gülden Gökçen AKKURT
Head of the Department of Energy Systems Engineering

Prof. Dr. Mehtap EANES
Dean of Graduate School of Engineering and Sciences

To Mehmet Çimen

ACKNOWLEDGEMENTS

First and foremost, I would like to express my deepest gratitude to my advisor, **Assoc. Prof. Dr. Başar Çağlar**, for his unwavering support, insightful guidance, and endless patience throughout the course of this thesis. His encouragement and mentorship have played a vital role not only in the completion of this work but also in my personal and academic growth. I am also sincerely grateful to my coadvisor, **Prof. Dr. Selahattin Yılmaz**, for his valuable contributions and perspectives during this process.

I would like to extend my heartfelt thanks to **Assoc. Prof. Dr. Yavuz Gökçe**, whose technical advice and open-door attitude allowed me to feel supported at every step. His willingness to share his knowledge and experience has been incredibly helpful throughout my experimental studies.

I gratefully acknowledge the support of MAK Savunma, whose contributions significantly facilitated the smooth execution of my experimental work. I would like to especially thank **Haydar Karatokuş** for his sincere support and assistance throughout this process.

I also sincerely thank the faculty members and research assistants of the Department of Energy Engineering at İzmir Institute of Technology for their continuous support, as well as the staff of İYTE-TAM Research Center for providing access to necessary facilities and their kind assistance during testing.

I am especially thankful to my dear friends Kevser Erdoğan, Dilara Çaygara, Ali Aras, Belka Anya, Yağmur Çetin, and Pelin Alaca, for their companionship, encouragement, and many shared moments that lightened even the most stressful days. Your presence has meant the world to me.

A special thank-you goes to **Mehmet Çimen**, who has stood by me not only during this thesis but throughout my entire academic journey. Your endless support, care, and belief in me have made all the difference.

Finally, I would like to express my deepest appreciation to my family. Their unconditional love, endless patience, and constant encouragement have been my greatest strength. I could not have come this far without them.

ABSTRACT

HEMP STEM-DERIVED ACTIVATED CARBON PRODUCTION AND PERFORMANCE ANALYSIS FOR SUPERCAPACITOR APPLICATIONS

In this study, activated carbon electrodes derived from hemp stem biomass were produced and optimized for supercapacitor applications using a systematic experimental design. The synthesis process combined controlled carbonization with chemical activation employing $ZnCl_2$ at varying temperatures (500–600 °C), activation times (1–3 h), and impregnation ratios (0.5–1 wt%). A Box-Behnken design and response surface methodology (RSM) were applied to determine the optimal activation parameters for maximizing specific capacitance and energy density. The resulting activated carbons were comprehensively characterized by BET surface area analysis, Raman spectroscopy, FTIR, SEM–EDX, and electrochemical measurements including CV, GCD, and EIS. The best-performing samples exhibited well-developed hierarchical porosity, moderate graphitic ordering (ID/IG up to 0.96), which enhanced ion transport and double-layer capacitance. The electrodes achieved a specific capacitance of up to 79.5 F/g at 0.5 A/g in a 0–1 V window, retaining about 78% of their initial capacity after 5000 cycles at 20 A/g, with coulombic efficiency maintained above 97%. The results demonstrate that hemp stems can serve as an efficient, sustainable precursor for producing high-performance porous carbon electrodes. The study highlights how fine-tuning thermal and chemical parameters effectively tailors the structural and electrochemical properties, providing valuable insights for developing biomass-derived supercapacitor materials.

ÖZET

SÜPERKAPASİTÖR UYGULAMALARI İÇİN KENEVİR SAPI KAYNAKLI AKTİF KARBON ÜRETİMİ VE PERFORMANS ANALİZİ

Bu çalışmada, kenevir sapı biyokütlesinden türetilen aktif karbon elektrotlar, sistematik bir deneysel tasarım kullanılarak süperkapasitör uygulamaları için üretilmiş ve optimize edilmiştir. Sentez süreci, kontrollü karbonizasyonu farklı sıcaklıklarda (500-600 °C), aktivasyon sürelerinde (1-3 saat) ve $ZnCl_2$/biomass ağırlık oranlarında (0.5-1) gerçekleştirilen kimyasal aktivasyonla birleştirmiştir. Özgül kapasitans ve enerji yoğunluğunu maksimize etmek amacıyla Box-Behnken tasarımı ve yanıt yüzey yöntemi (RSM) uygulanmıştır. Elde edilen aktif karbonlar, BET yüzey alanı analizi, Raman spektroskopisi, FTIR, SEM–EDX ve CV, GCD, EIS gibi elektrokimyasal ölçümlerle kapsamlı bir şekilde karakterize edilmiştir. En iyi performans gösteren örnekler, iyi geliştirilmiş hiyerarşik gözeneklilik ve orta düzeyde grafitik düzenlilik (ID/IG oranı 0.96'ya kadar) sergileyerek iyon taşınımını ve çift katmanlı kapasitansı artırmıştır. Elektrotlar, 0–1 V potansiyel aralığında 0.5 A/g akım yoğunluğunda 79.5 F/g özgül kapasitansa ulaşmış, 20 A/g akım altında 5000 çevrimden sonra ilk kapasitanslarının yaklaşık %78'ini korumuş ve coulombic verimlilik %97'nin üzerinde tutulmuştur. Sonuçlar, kenevir sapının yüksek performanslı gözenekli karbon elektrotlar üretmek için verimli ve sürdürülebilir bir öncü olabileceğini göstermektedir. Çalışma, termal ve kimyasal parametrelerin ince ayarının, yapısal ve elektrokimyasal özellikleri nasıl etkili şekilde şekillendirdiğini ortaya koyarak biyokütle kaynaklı süperkapasitör malzemelerinin geliştirilmesine yönelik değerli bilgiler sunmaktadır.

TABLE OF CONTENTS

LIST OF TABLES

Table **Page**

LIST OF FIGURES

Figure **Page**

CHAPTER 1

INTRODUCTION

1.1. Supercapacitors

The transition towards a sustainable, low-carbon energy future demands efficient and flexible energy storage technologies. Among various options, supercapacitors (SCs), also known as ultracapacitors or electrochemical capacitors, have emerged as a vital class bridging the gap between conventional capacitors and batteries.[1–4] Unlike batteries that rely primarily on bulk faradaic reactions, SCs store energy via non-faradaic electric double-layer mechanisms and/or fast surface faradaic processes, resulting in exceptionally high-power density, ultra-fast charge–discharge rates, and long cycle life that can exceed one million cycles.[5]

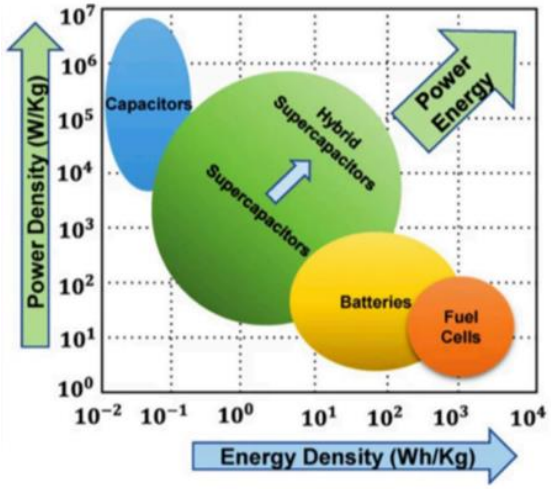

Figure 1. Ragone Plot for different energy storage technologies[5]

The position of supercapacitors within the energy storage spectrum is illustrated by the Ragone Plot in Figure 1, which shows SCs situated between capacitors and batteries. This unique placement makes SCs highly desirable for applications where rapid,

repeatable power bursts are essential, such as regenerative braking, power quality stabilization, and peak load compensation.[6]

1.1.1. Types of Supercapacitors

Supercapacitors are broadly classified into three main categories: Electric Double-Layer Capacitors (EDLCs), pseudocapacitors, and hybrid supercapacitors.[7,8]

Electric Double-Layer Capacitors (EDLCs) represent the most mature and commercially dominant form of supercapacitor technology, accounting for most devices used today.[5] Their core strength lies in their purely electrostatic charge storage mechanism: when a potential is applied, ions from the electrolyte form a compact double layer on the electrode surface without any faradaic redox reactions. This ensures rapid charge–discharge, extremely high reversibility, and exceptional long-term cycling stability.[9] The performance of EDLCs depends heavily on the surface area and pore architecture of the electrode material. Commercial activated carbons are widely favored due to their high specific surface area (800-2500 m^2/g), low cost, and tunable pore structure that supports ion transport. Advanced carbon materials such as graphene, carbon nanotubes (CNTs), and carbon aerogels offer even higher conductivities and customizable nanostructures that can enhance ion accessibility.[8] Despite their excellent power density (up to 10 kW/kg) and the ability to withstand more than 1 million charge–discharge cycles, EDLCs are limited by relatively low energy densities (~5–10 Wh/kg) due to their purely non-faradaic storage.[5]

Pseudocapacitors stand out for their ability to store significantly more energy than pure EDLCs by harnessing fast, reversible faradaic redox reactions on or near the electrode surface.[8] This additional faradaic mechanism enables much higher specific capacitance while still maintaining high-rate capability.

Typical pseudocapacitive materials include transition metal oxides (such as RuO_2, MnO_2, $Ni(OH)_2$) and conducting polymers (like polyaniline, polypyrrole, polythiophene). For instance, RuO_2 exhibits a theoretical specific capacitance exceeding 1200-1400 F/g, although practical values are lower due to conductivity losses and structural constraints.[5] MnO_2 is widely studied due to its abundance, low cost, and environmental friendliness, often reaching 200-300 F/g in real applications.

However, the main challenge with pseudocapacitors is mechanical stability. Repeated ion insertion and extraction during redox cycling can cause volumetric

expansion, cracking, or loss of active sites, which reduces long-term durability compared to EDLCs.[8] To overcome these issues, current research focuses on nanostructuring, doping, and hybrid composites that combine metal oxides with conductive carbon frameworks, merging high capacitance with improved stability. Pseudocapacitors find application in scenarios demanding higher energy storage than EDLCs alone, while still benefiting from rapid response times. For example, in high-power backup systems and hybrid storage modules. A typical EDLC and pseudocapacitor design are shown in Figure 2.

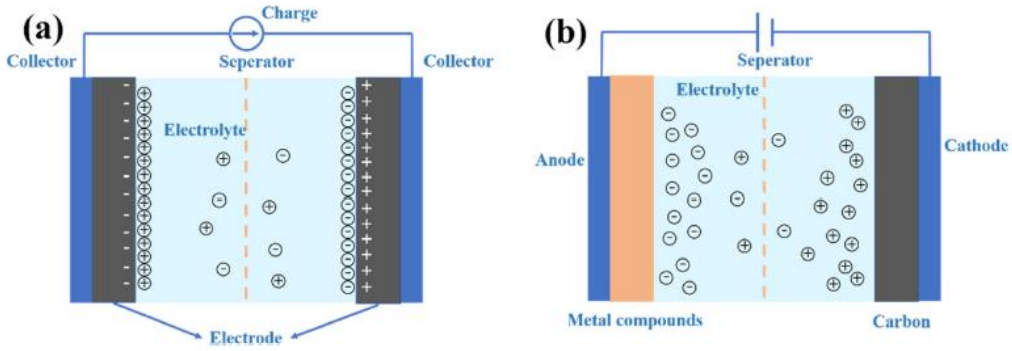

Figure 2. The schematic of (a) EDLC and (b) Pseudocapacitor design[5]

Hybrid supercapacitors (HSCs) represent the most promising direction for bridging the remaining gap between traditional supercapacitors and batteries by smartly combining the complementary strengths of EDLC and pseudocapacitive storage.[8] Unlike symmetric designs, HSCs typically adopt an asymmetric configuration where one electrode stores charge through non-faradaic double-layer capacitance (e.g., activated carbon) while the other exploits faradaic reactions (e.g., metal oxides, battery-type materials).

This dual mechanism enables HSCs to simultaneously achieve higher energy densities while retaining fast charge-discharge capability and robust cycle stability. Recent studies report energy densities up to ~40-60 Wh/kg with power densities exceeding 1-2 kW/kg, pushing HSCs closer to the practical performance of lithium-ion batteries but with far superior cycle life.[5]

Materials innovation has been critical for HSC development. Typical negative electrodes include transition metal oxides such as $Ni(OH)_2$, MnO_2, or $Li_4Ti_5O_{12}$, while carbon-based positive electrodes provide a large surface area for EDLC behavior.[8] In

addition to performance, HSCs offer design flexibility, they can be tailored for high-voltage asymmetric cells, flexible and wearable devices, and even integrated structural applications. Current research is exploring scalable production methods for commercial HSCs in electric vehicles, portable electronics, and grid-level modules that benefit from their high power-energy balance.

1.1.2. Electrode Materials

The performance of a supercapacitor depends strongly on the nature and quality of its electrode materials, as they determine the accessible surface area for charge storage, electrical conductivity, ion transport dynamics, and long-term cycling stability.[10] An ideal electrode should combine high surface area, hierarchical pore structure, good electrical conductivity, and stable electrochemical behavior during repeated charge–discharge cycles.

Carbon-based materials remain the most widely used electrodes for commercial EDLCs due to their high double-layer capacitance, good electrical conductivity, and chemical stability.[11] Activated carbon (AC) is the dominant choice because it provides high specific surface area (typically 800-2500 m^2/g), tunable micropore–mesopore networks, and low production cost. Commercial AC-based supercapacitors typically achieve specific capacitances of 80–200 F/g in aqueous electrolytes like 6 M KOH or H_2SO_4.[12] Beyond AC, advanced carbon nanostructures such as carbon nanotubes (CNTs) and graphene offer improved electrical pathways and faster ion transport, contributing to higher rate capability. For example, CNT-graphene composites can reach specific capacitances above 250 F/g due to their synergistic conductivity and accessible pore channels.[10]

Transition metal oxides are another important electrode family, utilized for pseudocapacitors because they enable fast surface redox reactions in addition to double-layer formation. Typical examples include MnO_2, RuO_2, NiO, and Fe_2O_3, which offer theoretical capacitances up to 1200–1400 F/g but often achieve 200–500 F/g in practice due to partial redox accessibility and low intrinsic conductivity.[13] For instance, MnO_2 electrodes with a flower-like nanostructure show 250-300 F/g at 1 A/g with good rate performance.[10] However, the main drawback is volumetric expansion during cycling, which can cause structural degradation and reduce cycle life compared to carbon electrodes.

Conducting polymers such as polyaniline (PANI), polypyrrole (PPy), and polythiophene (PTh) also store charge through fast faradaic reactions and deliver high specific capacitance, typically 300-600 F/g.[11] They are valued for their flexible film formation and easy processing at low temperatures. Yet, the repeated doping–dedoping process can lead to mechanical stress and cracking, limiting their lifetime. Recent advances combine conducting polymers with nanocarbon frameworks to enhance conductivity and structural integrity.

Hybrid electrodes, combining carbon materials with metal oxides or polymers, are being developed to merge high energy density with the excellent rate capability and stability of carbon.[10] For example, an AC–MnO_2 composite electrode can deliver 300-350 F/g by combining EDLC and pseudocapacitive effects. Similarly, graphene–PANI hybrids show improved cycling performance compared to pure polymer electrodes.

1.1.2.1. Activated Carbon Electrodes

Among carbon-based materials, activated carbon (AC) remains the principal electrode material for commercial supercapacitors due to its large surface area, well-developed pore structure, moderate conductivity, and economic feasibility.[14] It is commonly derived from a wide range of biomass feedstocks, including lignocellulosic residues such as coconut shells, sawdust, fruit stones, and textile waste.[15] Several studies list unconventional biomass precursors like soybean straw, tea waste, banana peels, or even eggshells, which have produced ACs with BET surface areas frequently exceeding 2000 m^2/g and specific capacitance values in the range of 300-400 F/g.[16,17]

Recently, hemp (*Cannabis sativa*) has gained particular attention due to its fast growth, high carbon yield, and sustainability credentials.[18] For instance, hemp stalks activated with KOH have demonstrated promising results, reaching specific capacitances around 260-270 F/g at 1 A/g with energy densities near 50-60 Wh/kg and stable cycle life.[19] Hybridizing hemp-derived AC with metal oxides such as MnO_2 or RuO_2 can further enhance the performance by combining the EDLC effect of carbon with pseudocapacitive redox sites.[14]

The general production route for AC involves pyrolyzing biomass under an inert atmosphere followed by an activation step. Physical activation uses oxidizing agents like steam or CO_2 at elevated temperatures (~700-900 °C), partially gasifying the char via

reactions like $C + CO_2 \rightarrow 2CO$, which expand the pore structure.[20] Chemical activation, in contrast, impregnates the char with agents like KOH, $ZnCl_2$, or H_3PO_4 and heats it at moderate temperatures (~400-800 °C).[15] For example, KOH reacts with carbon according to $6KOH + 2C \rightarrow 2K + 3H_2 + 2K_2CO_3$, intercalating potassium ions and creating new micropores while increasing the BET surface area up to 2500-3000 m^2. $ZnCl_2$ and H_3PO_4 mainly promote dehydration and aromatization, forming well-connected micro/mesoporous structures.[14] Overall, chemical activation often achieves higher surface areas and better pore development than physical methods alone.[17]

The choice of activation method strongly affects the final pore architecture and surface functionality. While steam or CO_2 activation favors narrow micropores, chemical agents like KOH or H_3PO_4 broaden the pore size and introduce surface oxygen-containing functional groups.[20] KOH-activated carbons typically feature –OH and –COOH groups, whereas $ZnCl_2$ activation may yield additional chlorine or phosphate species. Such functionalization not only tunes the pore size but also improves electrolyte wettability, which is vital for rapid ion transport. High microporosity is essential for large charge storage, but the presence of mesopores (often 20-50% of total pore volume) helps accelerate ion diffusion under high current conditions.[16]

1.1.3. Factors Effecting Activated Carbon Performance

Unique properties of carbon make it one of the best electrode materials for supercapacitors. Its high electrical conductivity, large surface area, and adjustable porosity enables fast charge transfer and plenty of electrochemical double-layer sites.[21] In practice, the performance of an activated carbon electrode depends on its pore structure, surface features, electrical conductivity, and surface chemistry, including how many heteroatoms are present.[22] Chemical activation methods such as $ZnCl_2$ or KOH help to tune these factors. Together, these physical and chemical features control how well ions move through the material and how they interact with the surface, which directly affects capacitance, energy and power density, and cycling stability.[14,23] This study focuses on optimizing these features for hemp-based activated carbon to boost its supercapacitor performance.

Pore structure and surface area: The pore network is key to how well activated carbon stores charge and move ions. Micropores smaller than 2 nm provide the most

surface area and are the main sites for ion storage in an electric double-layer.[14,21] More micropores usually mean higher specific capacitance.[23] Mesopores between 2 and 50 nm act like highways for ions, shortening the path and lowering resistance. This supports faster charging and higher power density.[22] Bigger macropores over 50 nm help the electrolyte flow deeper into the carbon but add less to capacitance.[14] For best results, a mix of all three pore types is ideal. For example, biomass carbons activated with $ZnCl_2$ often develop pores from 0.5 to 3 nm, giving a balanced micro–mesopore network that improves ion movement.[14] Most activated carbons have surface areas of several hundred to more than 1000 m^2/g.[22] A larger surface area means more charge can be stored. KOH activation of hemp, for example, increased the BET surface area from 280 to 1300.[14] This research aims to fine-tune activation conditions to control pore sizes and get the best surface area for hemp-based carbon.

Electrical Conductivity and Heteroatom Doping: High electrical conductivity helps electrons move quickly during charging and discharging.[21] Highly graphitized carbon or well-linked sp^2 structures lower internal resistance.[22] Biomass carbons often have a mix of graphitic and amorphous parts. Making carbon more graphitic, for example by using higher carbonization temperatures, can improve rate performance.[5] Adding heteroatoms like nitrogen, oxygen, sulfur, phosphorus, or boron can also boost performance. These atoms change how electrons are spread inside the carbon. Nitrogen, for instance, adds extra electrons and makes the surface more active.[21] This can raise capacitance and conductivity and add extra redox reactions[5]. Oxygen and sulfur groups also help ions stick to the surface. Some doping is good, but too much can damage the pore network and reduce conductivity. So, the activation steps must be balanced. This thesis tests different conditions to find the best setup that improves conductivity but keeps the pore structure strong.

Surface Chemistry and Electrode–Electrolyte Interface: Surface functional groups affect how the electrode and the electrolyte interact. Groups with oxygen (like –OH or C=O) or other heteroatoms improve wettability, helping the electrolyte spread fully through the pores.[14] Better wettability lowers resistance and lets ions reach more surface area, which increases the double-layer effect. Some groups, like phosphate units from phosphoric acid activation, can also add extra redox sites that boost capacitance.[23] A well-prepared surface allows a larger active area and faster ion movement, which means higher energy and power density. By adjusting these surface groups through careful activation,

this research aims to strengthen the interface and improve the total performance of hemp-derived carbon in supercapacitors.

1.1.4. Application of Experimental Design in Activated Carbon Production

The production of high-performance activated carbon critically depends on multiple process variables, such as precursor type, carbonization temperature, activation agent ratio, activation temperature, and residence time. To systematically investigate and optimize these variables, the use of experimental design techniques such as factorial design, response surface methodology (RSM), or Taguchi methods has proven highly effective. By applying a structured design of experiments (DOE), researchers can identify the key factors that most significantly influence crucial material properties, including specific surface area, pore size distribution, and electrochemical performance. For example, when producing biomass-derived activated carbon for supercapacitor electrodes, DOE approaches enable precise tuning of activation conditions (e.g., KOH or $ZnCl_2$ ratio, activation temperature) to maximize microporosity while minimizing undesirable structural collapse. Moreover, statistical models derived from experimental design facilitate the prediction of optimal production parameters with fewer experimental runs, saving time and resources while improving reproducibility. Overall, the integration of experimental design into activated carbon synthesis not only enhances material performance but also supports scalable and economically viable production strategies.

1.1.5. Objective and Content of the Thesis

The primary objective of this thesis is to develop sustainable, high-performance activated carbon derived from hemp stalks for application as an electrode material in supercapacitors. To achieve this goal, different activation methods and key process variables, such as carbonization temperature, chemical agent type and ratio, and activation time, are systematically optimized using response surface methodology (RSM). The study aims to investigate how these parameters influence the pore structure, surface chemistry, and electrochemical performance of the resulting carbon materials.

In addition to material synthesis, detailed physicochemical and electrochemical characterization methods are employed to evaluate the structural and functional properties of the produced activated carbons. Finally, the results are discussed in the context of existing literature to highlight the improvements and limitations compared to conventional activated carbons.

CHAPTER 2

LITERATURE REVIEW

The production of activated carbon from biomass is an increasingly important method for sustainable energy storage. This process generally involves four main stages[24]: pretreatment, carbonization, activation, and doping. In the pretreatment stage, biomass such as agricultural waste or woody residues is cleaned and shaped to the desired size. During carbonization, the biomass is heated under controlled conditions to break it down into a stable carbon structure. Activation, which can be chemical (using KOH, $ZnCl_2$, or H_3PO_4) or physical (using CO_2 or steam), further develops the pore network, increasing surface area and improving ion transport. Finally, doping with heteroatoms such as nitrogen, sulfur, boron, or phosphorus adjusts the surface chemistry and enhances electrochemical performance by enhancing capacitance and cycle stability.

A review of studies on hemp-based activated carbon shows that various methods and conditions have been explored for each of these stages. In carbonization, key parameters include temperature, duration, and heating rate, with both thermal and hydrothermal methods used. Hydrothermal carbonization is usually performed in autoclaves, while thermal methods typically use tubular reactors. In the activation stage, critical variables include activation temperature and time, the type and ratio of activating agent, and, for physical activation, gas flow rate. Doping parameters such as the type and amount of heteroatom also strongly affect the final material's electrochemical behavior. Therefore, carefully adjusting these variables is essential for improving both process efficiency and product quality.

In studies using hemp, hydrothermal carbonization has been common in the first step. Reported processes range from low temperatures (160-220 °C) for long durations (12-24 h) to higher temperatures (up to 800 °C) for shorter times, often followed by activation.[25–28]

For example, Kotsyubynsky et al.[29] examined how carbonization temperature affects the structure, morphology, and conductivity of porous carbon made from hemp

fibers. They carbonized fibers at 500–1000 °C, then treated the material with nitric acid (HNO_3) at 70 °C in nitrogen instead of a separate activation step. This treatment helped develop the pore network: surface area rose from 990 m^2/g to 1364 m^2/g as carbonization temperature increased, with the highest pore volume at 800 °C. A further heat treatment at 400 °C in air improved structural order. The study confirmed that carbonization temperature and HNO_3 treatment significantly affect electrical conductivity: at 800 °C, samples with acid treatment showed higher conductivity due to well-developed micro- and mesopores, reaching 10^{-3} S/m at low frequencies. Higher carbonization temperatures (up to 1000 °C) promoted graphitization and formed 3D networks that further improved conductivity, while lower temperatures (500-600 °C) led to weaker graphitization and lower conductivity.

Although these results show that temperature and acid treatment strongly affect structure and conductivity, it is notable that no activation step was used; instead, high carbonization temperatures were relied on. In processes that do include an activation step, such high temperatures may not be needed. However, few studies systematically examine carbonization time. Most experiments fix carbonization at one temperature and duration, then vary only activation conditions, meaning the specific effect of carbonization time on structure and performance remains unclear. This highlights the need for more detailed studies on how carbonization parameters, especially duration, influence the final properties of hemp-based activated carbon.

There is extensive research on the activation stage of biomass-derived carbons, covering both chemical and physical methods. For instance, Gunasekaran and Badhulika[30] explored physical activation using CO_2 and examined how activation time affects electrochemical properties. Hemp fibers were first carbonized at a relatively low temperature of 300 °C for 2 hours, then physically activated under CO_2 at 900 °C for 10-30 hours. The resulting HFPC-30 material reached a surface area of 1060 m^2/g with a well-developed micro–meso–macro pore structure. In a two-electrode symmetric supercapacitor, HFPC-30 showed a high specific capacitance of 600 F/g at 1 A/g, along with stable cycle performance retaining 85% of its initial capacitance after 10,000 cycles at 2 V. Although these results demonstrate the potential of CO_2 activation, the long activation times and high temperatures may limit scalability. Testing shorter durations and milder conditions could help make physical activation more practical.

In chemical activation, KOH is the most frequently studied activating agent for hemp-derived carbon. For example, Jiang et al. used hydrothermal carbonization followed by KOH activation to produce activated carbon (HSAC) from hemp stalks. Their HSAC-4 sample, made with a KOH/biomass ratio of 4:1 and activated at 800 °C, achieved a balanced micro–mesopore structure with a surface area of 865 m^2/g and showed 279 F/g at 0.5 A/g. It retained 91.6% of its initial capacitance after 5000 cycles. Similarly, Bembenek et al.[31] evaluated different KOH ratios and additional nitrogen doping. Their optimized K2-series samples achieved higher BET surface areas (up to 1678 m^2/g) and improved microporosity. After HNO_3 treatment and heat treatment, the best sample (KNO2) showed 245 F/g and 96% cycle stability after 10,000 cycles.

Further, Wang et al.[32] produced carbon spheres from hemp stalks using hydrothermal carbonization, pre-carbonization, and KOH activation at varying ratios. Their HACS-5 material, prepared with a 5:1 KOH/carbon ratio at 800 °C, reached a surface area of 3062 m^2/g and delivered a capacitance of 318 F/g with 96% retention after 10,000 cycles. However, high microporosity also increased ion diffusion resistance, suggesting that a more balanced pore structure might improve overall performance under high currents.

Sun et al.[26] compared hurd and bast parts of hemp. Using hydrothermal carbonization and KOH activation at 800 °C with different ratios, they found that hurd-derived carbons had higher surface area and better electrochemical properties than bast-derived ones. Their best sample, Hurd-a-5, showed 2879 m^2/g surface area and retained 83.9% capacitance even at high current densities, demonstrating promising energy (19.8 Wh/kg) and power densities (21 kW/kg).

Guo et al.[33] combined KOH and NH_3 in a single activation step to produce nitrogen-doped porous carbon (AKPC-750). The simultaneous activation and doping created a hierarchical micro–mesopore structure with a surface area of 1949 m^2/g and 4.4% nitrogen content. This material reached a specific capacitance of 352 F/g and maintained 96.3% retention after 10,000 cycles, while showing competitive energy density (99.5 Wh/kg) and power density (22,000 W/kg).

Despite these promising results, KOH activation has well-known limitations for commercial-scale production due to its strongly corrosive nature and the need for extensive post-treatment to neutralize residues.[34] This requirement not only raises production costs but also creates large volumes of alkaline wastewater, complicating

sustainable scale-up.[35] To address these issues, several studies on agricultural biomass such as rice husk, coconut shell, corncob, and nutshell have demonstrated that alternative activation agents, including zinc chloride and phosphoric acid, can produce activated carbons with comparable or superior pore structures while minimizing corrosivity and wastewater treatment demands.[34] However, comparable systematic research for hemp feedstocks remains limited. This gap highlights the potential to explore less corrosive chemical routes under milder conditions, which could provide a more cost-effective and environmentally feasible pathway for producing high-quality hemp-based activated carbon.

Activation temperature and activation duration are other critical parameters that have been systematically examined in the context of biomass-derived carbons. In the study by Tan et al.[25], the effect of different activation temperatures on the production of active carbon derived from sisal hemp (SHAC) and its physicochemical and electrochemical properties was comprehensively investigated. Sisal hemp was first hydrothermally treated at 180 °C for 24 hours in an autoclave using a 50% H_2SO_4 solution, then activated with KOH at 500-800 °C for 1 hour. The SHAC-600 sample exhibited optimal properties with a surface area of 1303.5 m^2/g and a total pore volume of 0.602 cm^3/g. Nitrogen adsorption-desorption analyses confirmed that the balanced micro- and mesoporous structures of SHAC-600 facilitate ion transport and energy storage. In electrochemical tests, SHAC-600 achieved a maximum specific capacitance of 517.2 F/g at 2 mV/s and maintained 212.6 F/g even at a high current density of 50 A/g. Lower activation temperatures (500 °C) produced underdeveloped pores, while higher temperatures (700-800 °C) caused structural collapse and loss of surface area, underscoring the importance of precise temperature control.

In addition to temperature, the methods and reactor types used during carbonization and activation also significantly affect both technical efficiency and economic feasibility. Many studies employ hydrothermal carbonization in pressurized autoclave reactors[25,30], which can yield high-performance materials but may pose challenges for scale-up due to elevated operational costs and process complexity.

Following the activation step, heteroatom doping has emerged as a widely adopted strategy for improving the electrochemical properties of biomass-based carbons. This approach modifies carbon's surface properties and pore network to enhance energy storage capacity. Single-atom doping introduces heteroatoms such as nitrogen, boron,

sulfur, or phosphorus, each tailoring the material's conductivity, wettability, or redox activity. For instance, nitrogen doping creates pyridine and pyrrole groups that enhance conductivity and structural stability, while sulfur doping increases the active surface area and ion transport capacity.[36] Furthermore, combining multiple heteroatoms (e.g., B/N or N/S) can generate synergistic effects that simultaneously boost energy density and cycling durability.

However, the success of heteroatom doping relies heavily on precise control of doping conditions. Improper doping can damage pore structure or lower conductivity, negating the intended benefits. Recent studies illustrate this risk: Chaparro-Garnica et al.[37] used a three-step method combining hydrothermal carbonization, H_3PO_4 activation, thermal treatment, and nitrogen doping. While the specific capacitance of the HTC_HR_450 material was initially 141 F/g, it slightly decreased to 124 F/g after post-treatment, yet full retention after 5000 cycles showed improved long-term stability. Similarly, Gunasekaran and Badhulika[36] demonstrated that hemp fiber-derived carbon doped with boron, nitrogen, and phosphorus (BNPC) achieved a high surface area (1555.5 m^2/g) and outstanding hydrogen storage capacity (360 mAh/g) with 99.7% retention after 10,000 cycles. The clear performance differences between undoped, singly doped, and multi-doped samples confirm that a synergistic approach can significantly improve electrical conductivity and pore accessibility, but only when the process is well-optimized.

In summary, although heteroatom doping and activation temperature control have proven effective for tailoring pore structure and boosting capacitance, existing studies mainly rely on corrosive activators such as KOH or multi-step processes with high energy input and long reaction times. Moreover, systematic, scalable pathways for combining mild activation, optimized doping, and less corrosive chemicals particularly for hemp stem-derived carbon remain limited. These gaps highlight the need for more practical, cost-effective, and environmentally sound methods, which this thesis aims to address through its integrated design-of-experiments approach.

Another method used to enhance the electrochemical and morphological properties of activated carbons is composite formation, which combines biomass-derived carbons with other functional materials to create synergistic effects. The composites reported in the literature include metal oxide–carbon composites (e.g., MnO_2, Co_3O_4, $NiCo_2O_4$), metal sulfide–carbon composites (e.g., MoS_2, NiS), phosphorus-doped carbon,

and conductive polymer–carbon hybrids (e.g., PPy, PANI). Metal oxides are valued for their high pseudocapacitance, metal sulfides enhance ion transport and charge transfer, phosphorus doping optimizes pore structure for higher energy density, and conductive polymers integrate carbon's large surface area with polymer conductivity, boosting overall performance. Multi-component hybrid composites such as carbon–metal oxide–metal sulfide combinations can further improve energy and power density through strong synergistic interactions. These approaches have significantly broadened the application potential of biomass-based carbons for advanced energy storage.[25,38]

For hemp-derived activated carbon specifically, various composite formation studies demonstrate how structural and electrochemical performance can be tuned. For example, Shi et al.[38] produced activated carbon from hemp fibers using a multi-step pretreatment, carbonization at 640 °C, KOH activation at 800 °C, and electrodeposition of Ni_3S_2 nanosheets. The resulting 3DHAC/Ni_3S_2 composite achieved a remarkable specific capacitance of up to 2797.43 F/g and retained 82.3% of its initial capacitance after 10,000 cycles, showing how metal sulfide decoration can dramatically enhance performance.

Tan et al.[25] demonstrated that forming a composite with MnO_2 nanoflakes on SHAC-600 improved the electrochemical behavior significantly. The MnO_2/SHAC-600 composite reached 397.9 F/g, and when assembled in an asymmetric supercapacitor with SHAC-600 as the negative electrode, it delivered an energy density of 46.2 Wh/kg and a power density of 3679.5 W/kg, maintaining 80.4% of its initial capacitance after 5000 cycles. Similarly, Yang et al. showed that integrating MnO_2 nanowires into hemp stalk-derived biocarbon resulted in a 3D MnO_2/HC composite that doubled the capacitance compared to pure biocarbon, reaching 340 F/g at 1 A/g and retaining 88% of capacitance at high currents. These results highlight the advantage of combining metal oxides with biomass carbon to improve both ion transport and pseudocapacitive contributions.

In another example, Jiang et al.[39] synthesized Fe_2O_3 nanoparticles with porous activated carbon (HAC) derived from hemp stalks. Despite a reduction in surface area due to nanoparticle loading, the Fe_2O_3/HAC composite showed clear synergistic effects, with a capacitance of 256 F/g -significantly higher than HAC or Fe_2O_3 alone- and excellent rate capability and cycling stability. These findings confirm that well-designed composite structures can compensate for individual material limitations by merging double-layer and pseudocapacitive behaviors.

However, despite these promising demonstrations, certain practical challenges remain. Many of these composite strategies involve multiple reaction steps, high temperatures, corrosive chemicals like KOH, and equipment such as autoclaves or vapor-phase reactors, all of which can limit scalability and increase production costs. In addition, KOH's highly corrosive nature raises environmental and operational concerns, especially for large-scale production, highlighting the importance of exploring alternative activation agents with lower corrosiveness and simpler handling. Studies on agricultural biomass such as coconut shell, nutshell, or rice husk have shown that milder activating agents like $ZnCl_2$ and H_3PO_4 can produce high-quality carbons with well-developed pore networks.[34] Still, systematic exploration of these alternatives for hemp stem feedstock remains sparse.

When these studies are examined collectively, it is clear that diverse methods and processing routes have been explored at every stage of the activated carbon production process. These approaches have yielded a wide range of performance outcomes but often rely on cost-intensive or corrosive steps that pose obstacles to industrial feasibility. Thus, designing realistic, economically viable, and environmentally friendly processes such as using milder chemicals, shorter reaction times, and integrated experimental design to systematically optimize conditions will be essential to unlock the full potential of hemp-based activated carbons for next-generation supercapacitors.

Based on this review, it is evident that biomass-derived carbon materials offer significant promises for sustainable energy storage due to their natural abundance and renewability. However, moving from laboratory demonstrations to industrial applications will require addressing the remaining gaps through more streamlined, scalable, and greener synthesis strategies.

CHAPTER 3

MATERIALS AND METHODS

3.1. Design of Experiment

In this study, Response Surface Methodology (RSM) was used to systematically investigate how activation parameters affect the electrochemical properties of hemp stem-derived activated carbon electrode. RSM enables the construction of empirical models to describe the relationships between independent variables (factors) and performance outputs (responses). The structured application of RSM involves the following steps:

(i) Selection of relevant factors and practical ranges

(ii) Planning and performing experiments using a structured design

(iii) Fitting a regression model to the experimental data

(iv) Checking the model adequacy using ANOVA and lack-of-fit tests

(v) Graphically interpreting the response surfaces to locate optimum operating points[40]

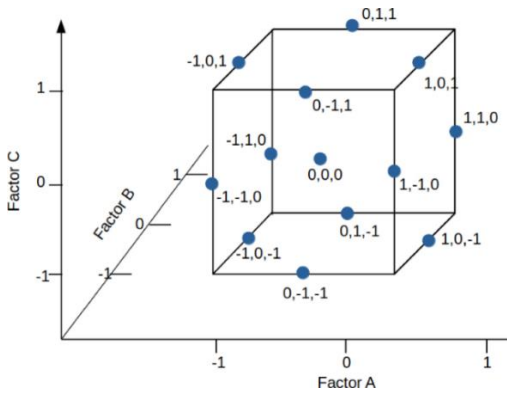

Figure 3. Schematic representation of a Box–Behnken Design for three factors[41]

A Box-Behnken Design (BBD) was selected for fitting second-order (quadratic) models. BBD designs are based on 3-level incomplete factorial arrangements. For three

factors, the experimental points are distributed at the midpoints of the edges of a cube together with the center points at the design center, as illustrated in Figure 3.

Three independent variables were defined as activation temperature (°C), activation time (h), and $ZnCl_2$/biomass impregnation ratio (w/w). Each factor was studied at three coded levels (−1, 0, +1) and two center points were included in the experimental matrix. The coded factor levels used in the design are summarized in Table 1.

Table 1. Coded factor levels used in the Box–Behnken Design

Factor	**Level (-1)**	**Level (0)**	**Level (+1)**
Activation Temperature (°C)	500	550	600
Activation Time (h)	1	2	3
$ZnCl_2$/Biomass Ratio (w/w)	0.5	1.0	1.5

Required number of runs (N) for a Box–Behnken Design is defined by Equation 1:

$$N = 2k(k-1) + C_0 \quad (1)$$

where k is the number of factors and C_0 represents the number of replicated center points included to estimate pure experimental error.

A total of 14 experimental runs were generated according to the BBD scheme, including the replicated center points. The coded experimental matrix used to implement the design is shown in Table 2, which illustrates the combination of factor levels used to develop the second-order response surface models.

Table 2. Combination of factor levels used to develop the second-order response surface models

Run	Temperature (A)	Time (B)	Ratio (C)
1	–1	–1	0
2	–1	+1	0
3	+1	–1	0
4	+1	+1	0
5	–1	0	–1
6	–1	0	+1
7	+1	0	–1
8	+1	0	+1
9	0	–1	–1
10	0	–1	+1
11	0	+1	–1
12	0	+1	+1
13	0	0	0
14	0	0	0

The general mathematical form of a second-order response surface model is given by Equation 2:

$$Y = \beta_0 + \sum_{i=1}^{k} \beta_i X_i + \sum_{i=1}^{k} \beta_{ii} {X_i}^2 + \sum_{i<j}^{k} \beta_{ij} X_i X_j \quad (2)$$

where Y is the predicted response, β_0 is the constant term, β_i is the linear coefficient, $\beta_{ii}$is the quadratic coefficient, and β_{ij} represent the interaction coefficients for factors X_i and X_j.

After designing the experiments, the adequacy and statistical validity of the developed models were rigorously evaluated. First, **analysis of variance (ANOVA)** was performed to test the overall model significance and the significance of linear, quadratic, and interaction terms at the **95% confidence level**. **Lack-of-fit (LOF)** tests were conducted to verify whether the fitted models sufficiently represented the observed data within the design space.

Following model validation, the main effects and two-factor interactions were visualized using main effect plots and interaction plots to identify possible synergistic or antagonistic relationships among the factors.

Finally, a **multi-response desirability function** approach was applied to determine the optimal combination of activation parameters for **simultaneously maximizing both specific capacitance and energy density**, ensuring a balanced and practical trade-off for the development of high-performance supercapacitor electrodes.

3.2. Experimental

3.2.1. Activated Carbon Production

Hemp stems, used as the biomass precursor, were collected in their raw form directly from local agricultural fields. The raw biomass was first washed thoroughly with deionized water and ethanol to remove surface impurities and any adhering dust or organic residues. After washing, the hemp stems were dried in a laboratory oven at 100 °C for 24 hours to ensure complete removal of moisture. The dried material was then ground into a fine powder using a laboratory-scale knife mill to reduce the particle size prior to sieving. The ground biomass was subsequently sieved using a 200 µm mesh on a mechanical sieve shaker (Retsch AS200 Basic, Germany) to obtain a uniform particle size fraction. After sieving, the biomass powder was thoroughly homogenized by mixing to ensure consistency in the subsequent activation steps. For simultaneous carbonization and chemical activation, **$ZnCl_2$** was selected as the activating agent. The required amount of $ZnCl_2$ was dissolved in deionized water and thoroughly mixed with the powdered biomass to achieve the desired impregnation ratios of **0.5, 1.0, and 2.0** (weight ratio of $ZnCl_2$ to biomass). The dried, impregnated biomass was subsequently transferred to a furnace for activation. Thermal activation was performed under a continuous flow of nitrogen gas (2 L/min) to provide an inert atmosphere and prevent unwanted combustion. The furnace was programmed to heat the samples at a controlled heating rate of **10 °C/min** until reaching the target temperatures (**500, 550, or 600 °C**), which were maintained for **1, 2, or 3 hours** according to the experimental design. After completion of the heat treatment, the furnace was allowed to cool naturally to room temperature under nitrogen atmosphere. The resulting activated carbon was lightly ground using a mortar and pestle and then washed several times with deionized water at **70 °C** to remove residual activating agent and any soluble by-products. Finally, the washed product was oven-dried at **105 °C** for 12 hours and stored in airtight containers for further physicochemical and electrochemical characterization.

3.2.2. Electrochemical Characterization

3.2.2.1. Electrode Preparation

To evaluate the electrochemical performance of the produced activated carbon samples, symmetric supercapacitor cells were fabricated using a two-electrode configuration. For electrode preparation, a slurry was prepared by mixing **85 wt% activated carbon**, **10 wt% carbon black** (as a conductive agent), and **5 wt% polyvinylidene fluoride (PVDF)** binder in **2 mL of N-methyl-2-pyrrolidone (NMP)** as the solvent. The prepared mixture was first **vortex-mixed** to ensure uniform dispersion and then subjected to a brief ultrasonic bath treatment to eliminate any remaining agglomerates and enhance slurry homogeneity. Prior to coating, the **bare stainless-steel discs (1 cm²)** were individually weighed to determine the precise mass loading of the active material. The homogeneous slurry was then applied onto the pre-weighed discs by **drop-casting**. After coating, the electrodes were dried overnight at **60 °C** in a vacuum oven to ensure complete solvent removal and strong binder adhesion. Representative images of the current collectors before coating and after electrode fabrication are shown in Figure 4.

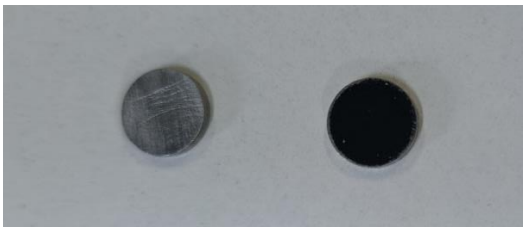

Figure 4. Current collectors before and after coating

3.2.2.2. Electrochemical Test Procedures

The dried electrodes were then assembled into symmetric cells using a **6 M KOH aqueous solution** as the electrolyte and a separator (**X**, specify type) positioned between the two electrodes to prevent short-circuiting and enable ion transport. All electrochemical measurements were performed at room temperature using a **Gamry**

Interface 1010 B potentiostat/galvanostat. The electrochemical test setup illustrated in Figure 5.

Figure 5. Electrochemical test setup

Electrochemical measurements, including **cyclic voltammetry (CV)**, **galvanostatic charge–discharge (GCD)**, and **electrochemical impedance spectroscopy (EIS)**, were systematically performed on all activated carbon samples to evaluate their capacitive performance under varying activation conditions.

Cyclic voltammetry experiments were performed over two distinct potential windows, **0-0.8 V** and **0-1.0 V**, to investigate the voltage-dependent charge storage characteristics of the electrodes. For each sample, CV scans were recorded at **six different scan rates**: **5, 10, 20, 50, 100, and 200 mV s^{-1}**, to observe the variation in current response and the shape of the voltammograms as a function of sweep rate. These measurements were primarily used to qualitatively assess the electric double-layer capacitor (EDLC) behavior, focusing on the rectangularity and symmetry of the CV curves, which indicate the reversibility and efficiency of ion adsorption and desorption at the electrode surface.

Galvanostatic charge–discharge measurements were performed within the same potential windows applied for CV (**0-0.8 V** and **0-1.0 V**) in order to determine the specific capacitance, energy density, and power density of the activated carbon electrodes under various current densities. For each sample, GCD tests were carried out at five different current densities: **0.5, 1, 5, 10, and 20 A g^{-1}**, enabling the evaluation of rate capability and coulombic efficiency at varying charge–discharge rates.

To assess the long-term electrochemical stability, a cyclic stability test was additionally conducted by subjecting the electrodes to **5000 charge-discharge cycles** at a fixed current density of **20 A g^{-1}** within the **0-0.8 V** window. Capacity retention (%) was calculated to quantify the change in specific capacitance between the lowest and highest current densities, illustrating the performance under practical high-power operating conditions.

The specific capacitance (**C$_s$**) of the electrodes was determined from the discharge curves using Equation 3:

$$C_s = \frac{I \times \Delta t}{m \times \Delta V} \tag{3}$$

where I is the discharge current (A), Δt is the discharge time (s), m is the total mass of active material in both electrodes (g), and ΔV is the effective voltage window (V) excluding the IR drop.

Energy density (**E**, Wh kg^{-1}) and power density (**P**, W kg^{-1}) were calculated using Equation 4 and Equation 5, respectively.

$$E = \frac{1}{2} C_s (\Delta V)^2 \tag{4}$$

$$P = \frac{E \times 3600}{\Delta t} \tag{5}$$

All GCD data were analyzed based on discharge profiles, and the resulting parameters were compared systematically across all activated carbon samples produced under different activation conditions.

Electrochemical impedance spectroscopy (EIS) measurements were performed over a frequency range from 0.01 Hz to 100 kHz using a 10 mV AC amplitude at open circuit potential (0V DC). Nyquist plots were obtained to examine the resistive, capacitive, and diffusive behavior of the electrodes. To interpret the impedance response

quantitatively, the experimental data were fitted to an equivalent circuit model (Figure 6) using Gamry Echem Analyst software.

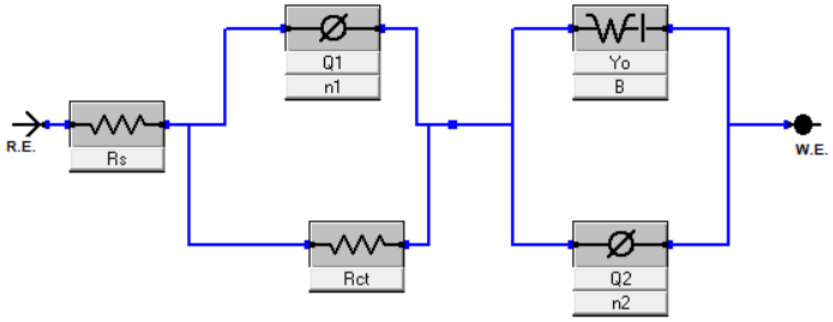

Figure 6. Equivalent circuit model used for EIS fitting

In this model, Rs represents the series resistance, which includes the intrinsic resistance of the electrode material, the electrolyte resistance, and the contact resistance within the cell. Rct denotes the charge transfer resistance, reflecting the resistance to faradaic or interfacial charge transfer processes occurring at the electrode–electrolyte interface. The two constant phase elements (CPEs), Q1 and Q2, are included to model the non-ideal capacitive behavior due to surface roughness, porosity, and heterogeneity of the carbon electrodes. The Warburg element, composed of the parameters Yo and B, accounts for the semi-infinite diffusion of ions within the porous structure of the electrode material. Together, this ECM configuration allows accurate fitting of the experimental Nyquist plots and enables the extraction of key resistive and capacitive parameters that reflect the material's ion transport and charge storage.

3.2.3. Physicochemical Characterization

Following the evaluation of the electrochemical test results, five representative activated carbon samples were selected for detailed physicochemical characterization based on their specific capacitance performance. These included the two best-performing samples (**AC600-1h-1r** and **AC600-3h-1r**), one average-performance sample (**AC550-2h-1r**), and the two lowest-performing samples (**AC550-3h-0.5r** and **AC500-2h-0.5r**). Comprehensive surface, structural, and elemental analyses were conducted exclusively

on these five samples to elucidate the correlations between physical properties and electrochemical behavior.

The morphological features and surface microstructure of the selected activated carbon samples were examined using a **FEI QUANTA 250 FEG scanning electron microscope (SEM)**. High-resolution SEM imaging was performed to observe the pore texture, particle morphology, and possible structural differences among the samples.

Elemental composition and distribution were analyzed using Energy Dispersive X-ray Spectroscopy (**EDX**) integrated with the SEM system. For each sample, EDX spectra were collected from three distinct regions to account for potential heterogeneity, and the resulting elemental data were averaged. The analysis focused on determining the relative atomic percentages of key elements (**C**, **N**, **O**, and **P**) associated with the carbon framework and dopants. Additionally, the presence of residual **Zn** and **Cl** was specifically monitored to assess the efficiency of the post-activation washing process and to detect any remaining activating agent or by-products.

The specific surface area and pore structure characteristics of the selected activated carbon samples were determined by nitrogen adsorption–desorption measurements conducted at **77 K** using a **Micromeritics 3Flex Surface Characterization Analyzer**. Prior to analysis, each sample was degassed at **300 °C for 12 hours** under vacuum to remove adsorbed impurities and moisture.

The specific surface area was calculated according to the **Brunauer Emmett–Teller (BET)** method using the adsorption data within the relative pressure range recommended by the instrument software. The complete adsorption–desorption isotherms were recorded to assess the type of porosity and to verify the development of micro- and mesopores. Pore size distribution and total pore volume were evaluated using the **Barrett Joyner Halenda (BJH)** method applied to the desorption branch of the isotherm.

Fourier-transform infrared spectroscopy (FTIR) measurements were performed to identify the surface functional groups present on the hemp stem-derived activated carbon samples. The spectra were recorded in the range of 4000-400 cm^{-1} using **Perkin Elmer Spectrum BX**.

The structural order and defect characteristics of the selected activated carbon samples were analyzed by Raman spectroscopy using a **Renishaw inVia Qontor Confocal Raman Spectrometer** equipped with a **532 nm laser source**. Spectra were

recorded over a Raman shift range from **800 cm^{-1} to 2400 cm^{-1}**, covering the prominent **D** and **G** bands characteristic of disordered and graphitic carbon structures, respectively.

The ID/IG intensity ratio was calculated to evaluate the degree of structural disorder and graphitization within each sample. This ratio serves as an indicator of defect density and was used for comparative analysis among the best, moderate, and least performing activated carbon samples selected based on electrochemical performance.

CHAPTER 4

RESULTS AND DISCUSSION

4.1. Design of Experiment (DOE)

This section provides a comprehensive overview of the experimental design framework developed to systematically investigate the effects of critical process parameters on the electrochemical performance of the synthesized activated carbon materials.

4.1.1. Factorial Structure and Experimental Matrix

In this subsection, the factorial structure and experimental matrix employed for the systematic investigation of process parameters are described in detail. The aim of implementing this design was to ensure that the combined and individual effects of the selected factors could be quantified with statistical confidence and translated into predictive models for the target electrochemical performance metrics.

The experimental plan was structured according to a Box–Behnken response surface design, which is recognized for its efficiency in fitting quadratic models while avoiding extreme factor combinations that may result in impractical or unstable experimental condition.[42] Three independent factors were selected based on their direct influence on the electrochemical properties of the produced activated carbon. Each factor was investigated at three coded levels to capture possible linear, quadratic, and interactive behaviors within a feasible operational window. The resulting factorial arrangement generated a total of **14 unique experimental runs**, including replicated center points to enable the estimation of pure experimental error and to enhance the reliability of the response surface models. The primary response variables measured for each run comprised **specific capacitance (F/g)**, **energy density (Wh/kg)**, **power density (W/kg)**,

and **capacity retention (%)**. The complete design matrix, together with the experimentally obtained values for these responses, is summarized in Table 3.

Table 3. Experimental design matrix and measured responses

Run	Temp (°C)	Duration (h)	Ratio ($ZnCl_2$/Biomass)	Specific Cap. (F/g)	Energy Density (Wh/kg)	Power Density (W/kg)	Capacity Retention (%)
1	500	1	1	34.89	2.68	196.4	44.80
2	500	2	1.5	40.51	2.63	177.7	69.20
3	600	2	0.5	31.36	2.71	265.8	30.08
4	550	1	0.5	31.60	2.69	253.9	38.07
5	600	1	1	59.04	5.17	239.3	22.15
6	600	2	1.5	36.63	3.17	263.2	41.98
7	600	3	1	58.11	5.08	321.67	41.46
8	550	2	1	41.02	3.38	248.6	44.37
9	500	2	0.5	10.10	0.78	182.2	45.72
10	500	3	1	36.48	2.56	304.5	85.55
11	550	1	1.5	58.15	4.99	324.9	53.91
12	550	3	1.5	33.08	2.62	227.0	43.80
13	550	3	0.5	29.66	2.47	274.7	39.73
14	550	2	1	40.71	3.50	244.3	28.00

The factorial structure and matrix thus form the foundation for the subsequent statistical analysis, which includes model adequacy assessment, main effects evaluation, interaction term significance, and the determination of reliable operating conditions, as elaborated in Sections 4.1.2 to 4.1.4.

4.1.2. Analysis of Variance (ANOVA) and Model Adequacy

This subsection presents the results of the analysis of variance (ANOVA) conducted to assess the statistical significance and adequacy of the response surface models developed for the primary electrochemical performance indicators. The ANOVA

outcomes provide critical insight into the extent to which the selected activation parameters and their interactions account for the observed variation in the target responses. A summary of the main model fit parameters is given in Table 4, which includes the coefficients of determination (R^2), adjusted R^2 (Adj. R^2), predicted R^2 (Pred. R^2), model significance (p-value), and lack-of-fit test results. The complete ANOVA tables, including detailed sum of squares, mean squares, F-ratios, and individual term significance levels, are provided in Appendix A for reference.

Table 4. Summary of the main model fit parameters

Response	**R^2 (%)**	**Adjusted R^2 (%)**	**Predicted R^2 (%)**	**Model p-value**	**Lack-of-Fit p-value**
Specific Capacitance	91	71	0	0.080	0.020
Energy Density	92	74	53	0.066	0.088
Power Density	62	0	0	0.678	0.038
Capacity Retention	76	22	0	0.392	0.500

For specific capacitance, the high R^2 value (~91%) indicates that a significant portion of the variation is explained by the model terms. However, the noticeable drop to an adjusted R^2 of approximately 71% and the near-zero predicted R^2 imply that some of the quadratic and interaction terms may be statistically non-significant, resulting in limited generalizability beyond the tested design interval. The energy density model shows a similar pattern, with an R^2 of ~92% and an adjusted R^2 of ~74%. The predicted R^2 (53%) indicates better generalizability than that of specific capacitance. By contrast, the models for power density and capacity retention exhibit modest R^2 values (~62% and ~76%, respectively) but show negligible adjusted and predicted R^2 values, indicating that the selected activation factors do not adequately account for the variation in these responses under the current parameter ranges.

Analysis of variance (ANOVA) indicated that not all quadratic models developed for the response variables were statistically significant at the 95% confidence level. The model for specific capacitance was found to be marginally significant (model $p = 0.080$), its linear component was statistically significant ($p = 0.041$). A similar trend was observed for the energy density model, which also exhibited marginal significance overall (model

p = 0.066), with a significant linear term (p = 0.027). In contrast, the models for power density (p = 0.678) and capacity retention (p = 0.392) were not statistically significant, suggesting a lack of predictive reliability for these responses within the quadratic framework.

To further assess model adequacy, lack-of-fit (LOF) tests were performed. The specific capacitance and power density models both exhibited significant lack of fit (p = 0.020 and 0.038, respectively), indicating that the quadratic models do not fully capture the underlying trends of the experimental data. In the case of specific capacitance, the pure error was exceptionally low (0.05) due to nearly identical replicate values at the center points, which may have artificially inflated the LOF statistics. A significant LOF, in this context, implies that model deviations exceed the level of inherent process variability or that the variability was underestimated. The LOF result for the energy density model was near the threshold of significance (p = 0.088), while the capacity retention model showed no significant lack of fit (p = 0.500), implying that although its overall fit was weak, it does not exhibit systematic bias in modeling the average trend.

$$\textbf{SC (F/g)} = -376 + 0.92T - 14.3t + 258.7R + 0.00044T^2 + 7.37t^2 - 40.4R^2 - 0.0126Tt - 0.251TR - 11.57tR \quad (6)$$

$$\textbf{ED (Wh/kg)} = -159 + 0.458T - 7.0t + 65.4R + 0.000311T^2 + 2.35t^2 + 12.92R^2 + 0.0004Tt - 0.0501TR - 3.87tR \quad (7)$$

where T is temperature (°C), t is activation duration (h), and R is the impregnation ratio.

Accordingly, the detailed analysis of factor effects, interaction plots, and final condition selection focuses exclusively on specific capacitance and energy density. Nevertheless, for the sake of transparency and completeness, the full ANOVA outputs, including the statistical details for power density and capacity retention, are provided in Appendix A.

Based on the ANOVA results, the final quadratic regression models were established in Equation 6 and equation 7 for the specific capacitance (SC) and energy density (ED) responses, respectively.

These equations confirm that the factor effects and interaction terms captured by the models can adequately describe the variation in the specific capacitance and energy density responses within the tested design space. The main and interaction effects derived from these models are discussed in detail in Section 4.1.3.

4.1.3. Analysis of Main Effects and Interactions

This section presents an analysis of the influence of three activation parameters - activation temperature (°C), activation duration (h), and $ZnCl_2$ impregnation ratio (mass ratio of $ZnCl_2$ to biomass)- on the specific capacitance and energy density of activated carbon.

4.1.3.1. Effects on Specific Capacitance

Main effects plot for specific capacitance is shown in Figure 7. An increase in activation temperature from 500 °C to 600 °C significantly enhances specific capacitance, with values rising from approximately 20-30 F/g at 500 °C to about 50-60 F/g at 600 °C. In contrast, activation duration shows a non-monotonic effect: capacitance decreases slightly at an intermediate duration of 2 hours (~40 F/g), while both shorter (1 h) and longer (3 h) durations yield higher values in the range of 45–50 F/g.

The $ZnCl_2$ impregnation ratio also plays a decisive role. Increasing the ratio from 0.5 to 1.0 results in a clear improvement in specific capacitance due to enhanced pore development, but a further increase to 1.5 does not provide additional benefit and instead causes a slight decline. This indicates an optimal $ZnCl_2$ ratio near 1:1, beyond which excessive chemical activation may deteriorate the carbon structure or cause pore collapse, ultimately reducing performance.

These parameters also demonstrate significant interaction effects shown in Figure 8. The combined effect of activation temperature and duration shows that at 500 °C,

extending the activation time from 1 to 3 hours markedly improves capacitance. At 600 °C, however, even a short duration of 1 hour yields high capacitance, and prolonging the time provides only slight improvement. This demonstrates that activation time is more influential at lower temperatures, whereas higher temperatures reduce the process's sensitivity to duration. This convergence of the duration curves at 600 °C and their wider separation at 500 °C clearly demonstrate that longer activation times are necessary at lower temperatures to achieve high capacitance, whereas higher temperatures make extended durations less critical.

A similar pattern appears in the interaction between activation temperature and the $ZnCl_2$ ratio. At 500 °C, using a low ratio (0.5) results in low specific capacitance, but increasing the ratio up to 1.5 significantly enhances performance because more activating agent creates more porosity. At 600 °C, however, even samples with a low ratio achieve relatively good capacitance, and increasing the ratio further provides only a modest improvement. This indicates that at lower temperatures, the chemical ratio plays a more critical role, while at higher temperatures, the thermal effect alone is sufficient to compensate for a lower $ZnCl_2$ content.

The interaction between activation duration and the $ZnCl_2$ ratio also reveals a synergistic effect. At a short activation time of 1 hour, increasing the $ZnCl_2$ ratio results in only moderate improvements in capacitance because the limited duration restricts the full effect of the activating agent. In contrast, when the activation time is extended to 3 hours, a higher ratio produces a much more substantial increase in capacitance, with the best performance observed when both parameters are maximized. This trend is evident from the wider separation of the ratio curves at 3 hours compared to 1 hour. Because the lines do not intersect, a higher ratio always results in better performance, but the level of improvement is clearly influenced by how long the activation is carried out.

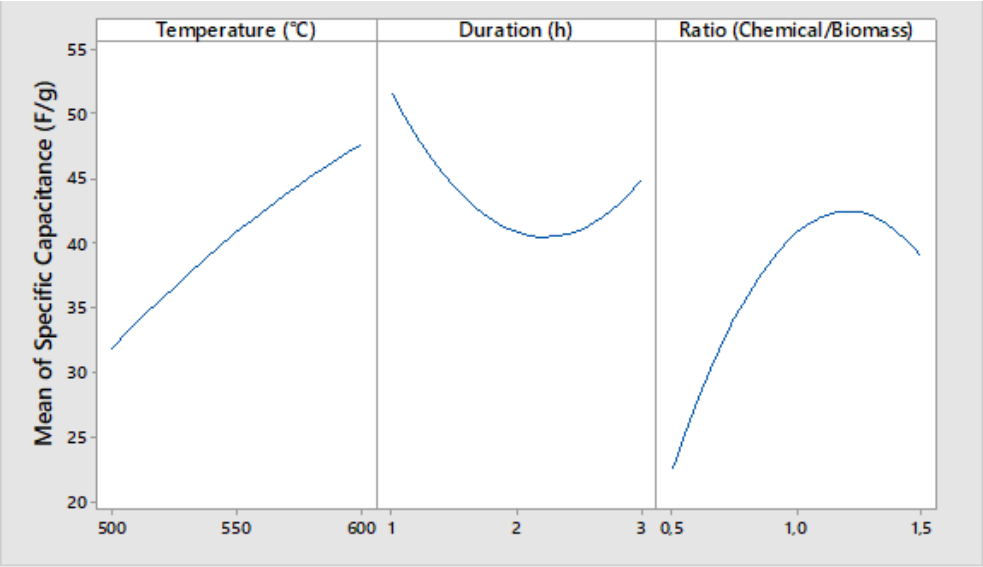

Figure 7. Main effects plot for specific capacitance

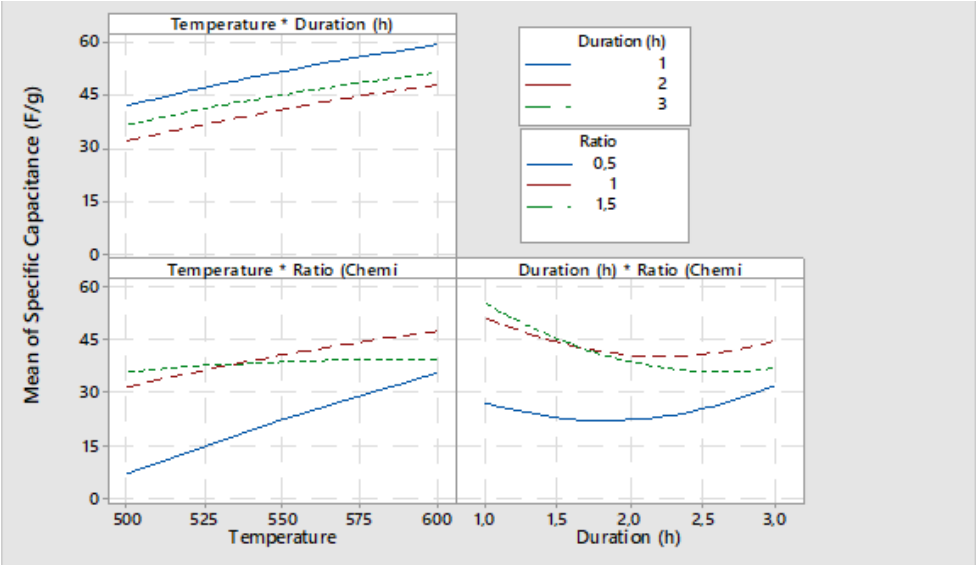

Figure 8. Interaction plot for specific capacitance

4.1.3.2. Effects on Energy Density

Main effects plot for energy density is shown in Figure 9. An increase in activation temperature was found to have a clear positive effect on energy density. Raising the temperature from 500 °C to 600 °C increased the energy density from approximately 2-2.5 Wh/kg to around 4-4.5 Wh/kg, which aligns with the trend observed for specific capacitance. Regarding activation duration, the energy density showed a non-linear, U-shaped response: the highest values (~4.4 Wh/kg) were achieved with a short activation time of 1 hour. At 2 hours, energy density dropped to its lowest point (~3.4 Wh/kg) but partially recovered to about 3.8 Wh/kg when the duration was extended to 3 hours. This pattern suggests that an intermediate activation time may negatively affect the pore structure, possibly due to partial collapse or excessive widening of micropores, which limits charge storage capacity. In contrast, a short activation helps preserve a favorable pore structure, while longer times beyond 2 hours may encourage the formation of mesopores or a more developed porous network, partly restoring energy density.

Similarly, the $ZnCl_2$ impregnation ratio showed a clear optimum for energy density. Increasing the ratio from 0.5 to about 1.0 significantly improved performance, raising energy density from 2 Wh/kg to 3.5 Wh/kg. However, increasing the ratio further to 1.5 caused a slight decline (~3.2 Wh/kg). This indicates that while an adequate amount of activating agent is needed for effective pore development, too much chemical activation can damage the structural integrity of the carbon. Overactivation may lead to the formation of excessively large pores or the loss of the conductive carbon framework, both of which reduce the effective surface area and conductivity, ultimately limiting energy storage performance.

The interaction plots for energy density (Figure 10) indicate generally weaker interactions compared to the other responses, as the lines are mostly parallel, showing that the factors have primarily independent additive effects. The combined effect of activation temperature and duration revealed no significant synergy or antagonism, which is evident from the nearly parallel lines in the plot. At both temperature levels, the same pattern was observed: a 1-hour activation produced the highest energy density, 3 hours gave moderate values, and 2 hours consistently resulted in the lowest performance. This consistent trend across temperatures confirms that increasing temperature raises energy

density overall but does not change how activation time influences it. In other words, the U-shaped behavior of energy density with respect to activation time (optimal at 1 h and lowest at 2 h) remains valid regardless of temperature. The parallel nature of the lines implies that temperature mainly shifts energy density upward without altering the time-related effect.

A similar observation applies to the interaction between activation temperature and the $ZnCl_2$ ratio. The nearly parallel lines indicate that temperature and chemical ratio affect energy density independently. At both 500 °C and 600 °C, increasing the $ZnCl_2$ ratio from 0.5 to 1.0 significantly improved energy density, while increasing it further to 1.5 caused a slight decline. This trend being the same at both temperature levels suggests that the influence of $ZnCl_2$ ratio is not affected by temperature. The uniform improvement in energy density with higher temperature across all ratios further supports the absence of a strong interaction between these two factors.

In contrast, the interaction between activation duration and $ZnCl_2$ ratio showed a moderate effect, mainly due to the non-linear time response. At a short activation time of 1 hour, increasing the ratio raised energy density, with 1.0 being optimal. However, at 2 hours where energy density was at its minimum this positive effect was reduced, and all ratio levels resulted in similarly low values. When the duration was extended to 3 hours, energy density increased again, especially at higher ratios, and performance at 3 hours with a 1.5 ratio nearly matched the 1-hour result at a 1.0 ratio. Although the optimum ratio did not shift, the degree of its positive effect increased with longer activation times. This suggests that the benefit of a higher $ZnCl_2$ ratio depends on sufficient activation time, allowing the chemical agent to fully develop the pore structure.

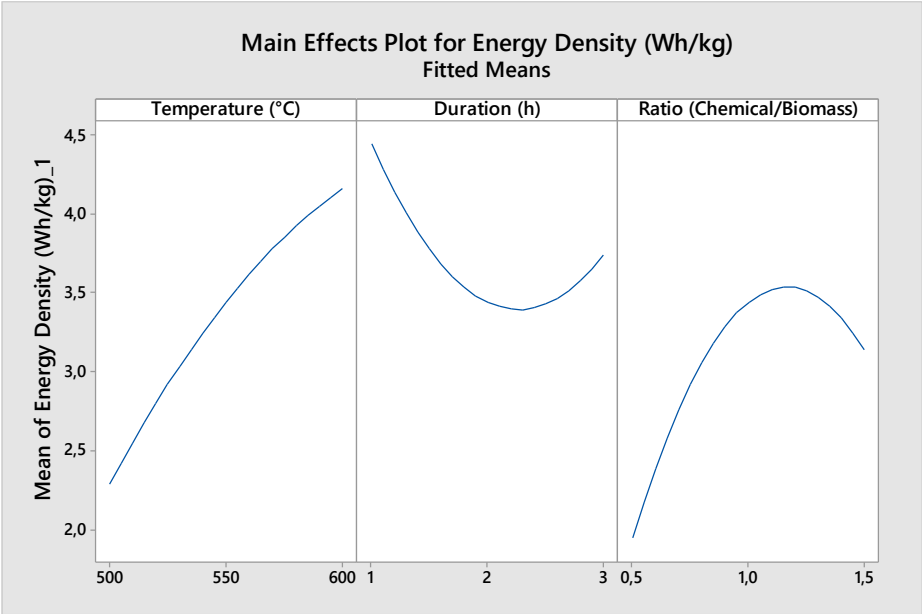

Figure 9. Main effects plot for energy density

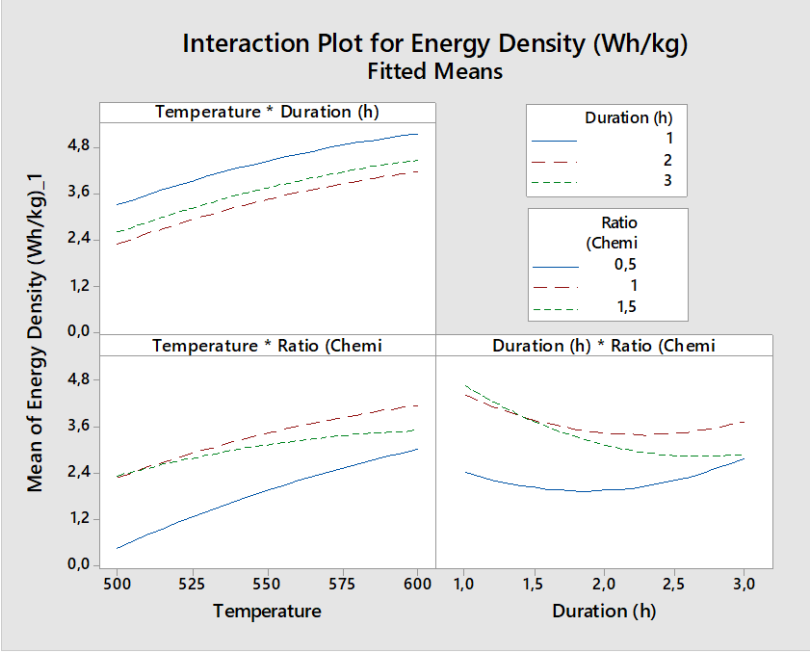

Figure 10. Interaction plot for energy density

4.1.4. Multi-Response Optimization and Validation

Based on the quadratic regression models previously defined for specific capacitance and energy density (see Equations 1 and 2), a multi-response optimization study was conducted to identify the most suitable activation conditions for hemp stem-derived activated carbon. Using the desirability function approach within the response surface methodology (RSM), the simultaneous maximization of both key responses was targeted.

Table 5. Predicted optimum values for specific capacitance and energy density with standard errors and 95% confidence intervals

Response	Predicted Value	Standard Error	95% CI Lower	95% CI Upper
Specific Capacitance (F/g)	60.4	6.37	42.7	78.1
Energy Density (Wh/kg)	5.3	1.5	3.8	6.8

The results indicate that an activation temperature of **600 °C**, a duration of **1 hour**, and a chemical agent-to-biomass ratio of **1.19** ($ZnCl_2$/biomass, w/w) yield the most favorable performance outcomes. According to the model predictions, these conditions are expected to achieve a specific capacitance of approximately **60.4 F/g** and an energy density of **5.3 Wh/kg**. The predicted optimum values, standard errors, and confidence intervals for the valid responses are summarized in Table 5. The associated standard errors for these predictions (6.37 F/g and 1.5 Wh/kg) are considered acceptable for laboratory-scale experimental planning, supported by the reasonably narrow 95% confidence intervals.[43,44]

4.2. Electrochemical Analysis

Among the samples investigated in design of experiments, 5 active carbons obtained at different experimental conditions were selected for further electrochemical and physicochemical analysis. The selectin was made based on their specific capacitance values, 2 for the best, 2 for the worst and 1 for intermediate performances. Results for other samples given in Appendix B. In the following section, their detailed characterization results are presented in the following sections.

4.2.1. Cyclic Voltammetry (CV) Analysis

The electrochemical performance of the activated carbons was systematically evaluated using cyclic voltammetry under different scan rates and voltage windows. The representative CV results are presented in Figure 11 (0-0.8 V) and Figure 12 (0-1.0 V), each showing the effect of scan rate on the capacitive behavior of the selected samples.

At the lowest scan rate of 5 mV/s, the CV curves (Figure 11(d)) are close to rectangular in shape, indicating ideal electric double-layer capacitor (EDLC) behavior with minimal resistive distortion. This form shows that ions can adsorb and desorb quickly and reversibly on the porous carbon surfaces, which is especially clear for AC600-1h-1r and AC600-3h-1r. Expanding the voltage window to 0-1.0 V (Figure 12(d)) increases the CV area for all samples, demonstrating higher charge storage capacity within the wider range. The CV profiles remain close to a rectangular and symmetric shape at 5 mV/s in the 1.0 V window, suggesting that the activated carbon electrodes, especially AC600-1h-1r, can operate stably up to 1.0 V in aqueous KOH without significant faradaic reactions. Only slight deviations from this shape appear near the higher voltage limit, likely due to oxidation of some impurities or IR drop close to water's decomposition point. Overall, at slow scan rates the samples mainly show capacitive behavior, and the absence of redox peaks in Figure 11(d) and Figure 12(d) confirms that charge storage is based on the electrostatic double-layer mechanism.

As the scan rate increases, the CV curves gradually move away from the ideal rectangular form and the enclosed area decreases, showing that less capacitance is accessible at higher rates. At 50 mV/s (Figure 11(c) and Figure 12(c)), the curves for

AC600-1h-1r and AC600-3h-1r still keep a mostly rectangular shape but with rounded corners and a slight tilt, especially in the wider voltage range. This change happens because higher scan rates increase internal resistance and make ion movement more difficult. Because ions cannot move fast enough at high scan rates, some parts of the porous structure, especially deeper micropores are not fully used. This causes the CV area to decrease and the curve to tilt more due to higher resistance.

At 100 mV/s (Figure 11(b) and Figure 12(b)), these effects become more noticeable as the loops tilt further but still maintain an approximately rectangular shape, indicating good rate capability. At the highest scan rate of 200 mV/s (Figure 11(a) and Figure 12(a)), all samples show clear distortion; the curves become lens shaped. This is expected because ion diffusion is strongly limited at this speed, so mainly the outer surface and larger pores contribute to charge storage, while the micropores cannot respond quickly enough. Notably, AC600-1h-1r still shows measurable capacitive current at 200 mV/s, while AC500-2h-0.5r exhibits very low current, indicating mostly resistive behavior. The fact that AC600-1h-1r retains some rectangular shape even at 200 mV/s suggests that its pore structure allows faster ion transport, which is important for high-power applications.

These results confirm that the scan rate strongly affects capacitive behavior. Rate capability, which means how well capacitance is kept at fast charge-discharge is clearly different among the samples. For example, the CV area of AC600-1h-1r and AC600-3h-1r only decreases moderately from 5 to 100 mV/s, while AC500-2h-0.5r drops sharply. This shows differences in pore design and conductivity. Carbons with hierarchical porosity combining micropores for high surface area with mesopores or macropores (see section 4.3.1.) for easy ion pathways maintain better capacitance at high rates. This structure shortens ion diffusion paths and lowers resistance, supporting charge storage even under fast cycling. In summary, all hemp-derived carbons show ideal EDLC behavior at low scan rates. Although capacitance drops at higher rates, materials like AC600-1h-1r and AC600-3h-1r have better rate capability, keeping a larger part of their low-rate capacitance up to 100-200 mV/s.

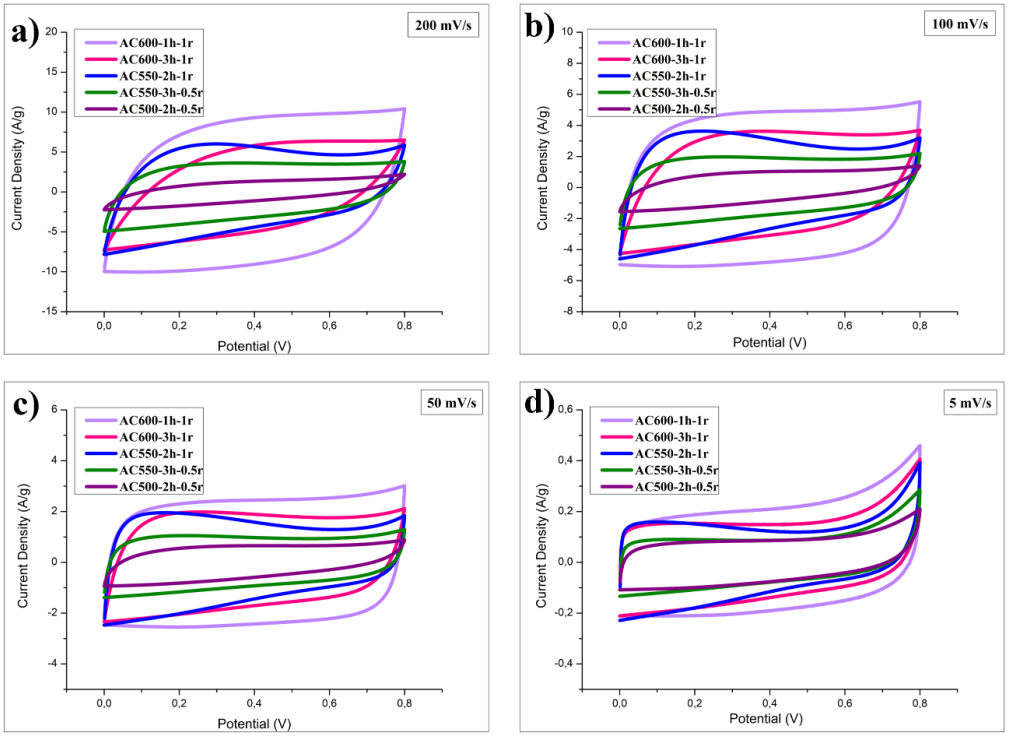

Figure 11. Cyclic voltammetry curves of activated carbons at 0-0.8V for scan rates a)200mV/S, b) 100mV/s, c) 50mV/sand d)5mV/s

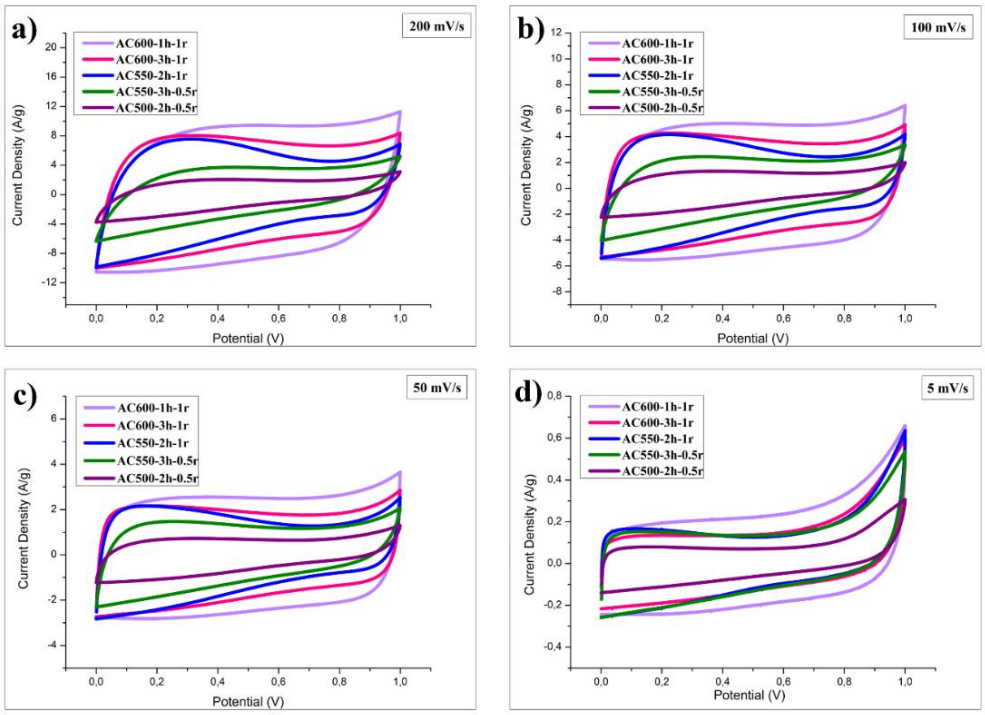

Figure 12. Cyclic voltammetry curves of activated carbons at 0-1.0V for scan rates a)200mV/S, b) 100mV/s, c) 50mV/sand d) 5mV/s

4.2.2. Electrochemical Impedance Spectroscopy (EIS) Analysis

The Nyquist plots (Figure 13) obtained for the selected hemp-derived activated carbon samples provide additional insights into the internal electrochemical behavior and strongly reinforce the equivalent circuit model (ECM) results. Specifically, the high-performing AC600-3h-1r and AC600-1h-1r electrodes exhibit small high-frequency intercepts (Rs ~2-5 Ω) and minimal semicircular regions in the mid-frequency range, directly confirming their low charge transfer resistances (Rct ~3.7-5.5 Ω) and excellent electrical conductivity. The nearly vertical tails at low frequencies further indicate efficient ion diffusion pathways and ideal capacitive behavior, which align well with their high specific capacitance, stable cycling performance, and well-developed pore structures (see Section 4.2.1). In contrast, the low-performing AC500-2h-0.5r sample shows a significantly larger semicircular arc and broader intercept (~4-5 Ω) with a less steep tail, reflecting its high Rct (~21 Ω) and notable ion transport limitations due to its poorly developed porous architecture (see Section 4.2.3). The intermediate samples AC550-3h-0.5r and AC550-2h-1r reveal moderate intercepts and clearly defined semicircular profiles, supporting their mid-range Rct values (~8–21 Ω) and indicating partially restricted charge transfer and ion mobility, which is consistent with their moderate pore interconnectivity observed in the BET and morphological analyses (see Section 4.3.1). Collectively, the Nyquist profiles strongly validate the fitted ECM parameters and clearly illustrate how the synergistic balance between pore structure, ion diffusion, and interfacial kinetics governs the overall electrochemical performance of these hemp-derived supercapacitor electrodes.

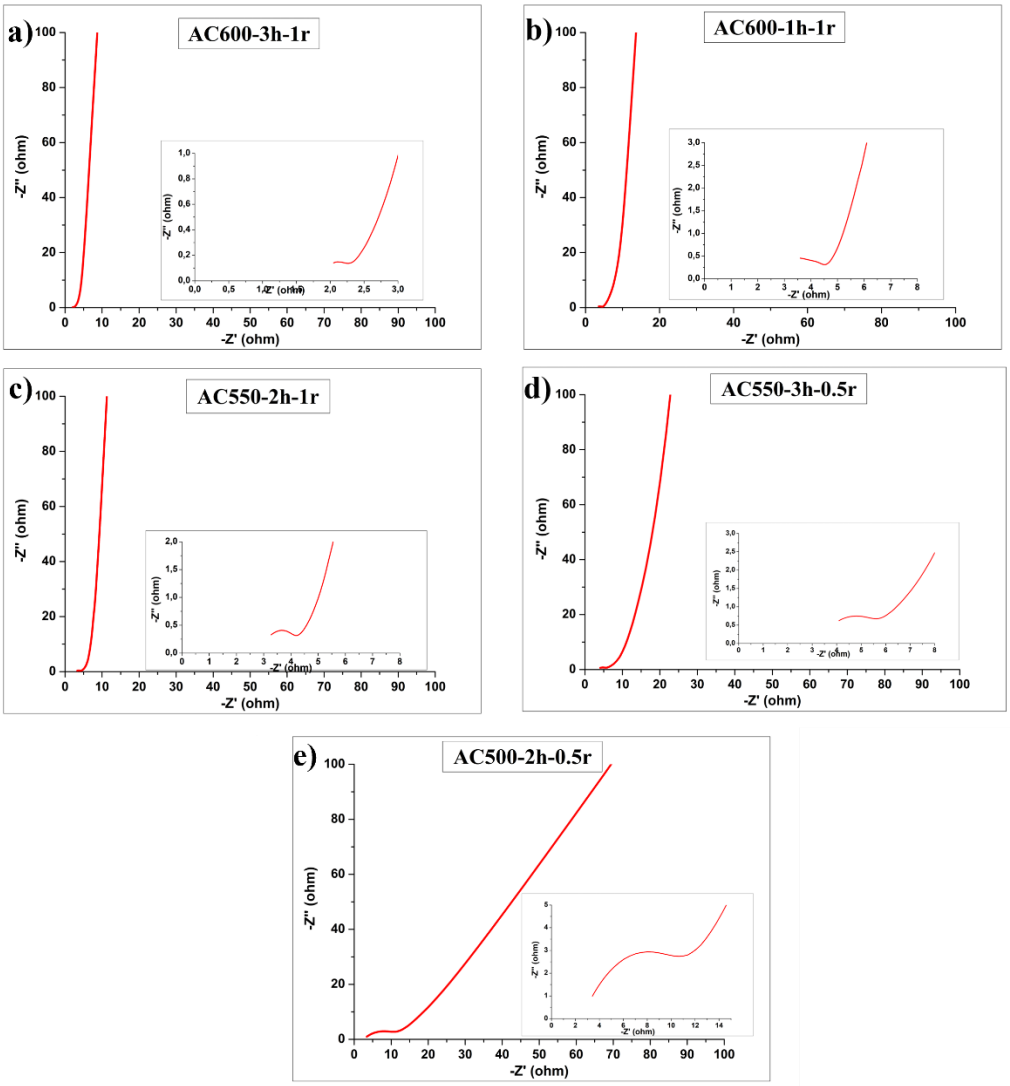

Figure 13. Nyquist plots of hemp-based activated carbon electrodes with inset details of the high-frequency region

4.2.2.1 Equivalent Circuit Model Interpretation of EIS Results

The equivalent circuit model (ECM) results provide clear evidence of how the internal resistive and capacitive elements vary across the synthesized hemp-derived activated carbon electrodes and are physically realistic when benchmarked against comparable biomass-based systems. Specifically, the high-performing AC600-1h-1r and AC600-3h-1r samples exhibit low series resistance (Rs = 2.256 Ω and 5.341 Ω, respectively) and low charge transfer resistance (Rct = 5.521 Ω and 3.673 Ω), indicating sufficient electrical conductivity and fast interfacial kinetics. Their Warburg parameters (B = 800 × 10^{-3} and 380 × 10^{-3} $s^{1/2}$) and constant phase elements (Yo = 22.88 × 10^{-3} and 121.9 × 10^{-3} $S \cdot s^{1/2}$) confirm balanced ion diffusion through well-developed hierarchical pores, which is fully consistent with the BET surface area and pore size distribution results (see Section 4.3.1).

Table 6. Equivalent Circuit Model (ECM) fitting parameters

Sample	**Rs (Ω)**	**Rct (Ω)**	**Yo ($S \cdot s^{1/2}$)**	**B ($s^{1/2}$)**
AC550-2h-1r	2.041	21.51	20 × 10^{-3}	72.47 × 10^{-3}
AC600-1h-1r	2.256	5.521	22.88 × 10^{-3}	800 × 10^{-3}
AC550-3h-0.5r	3.818	8.321	15.32 × 10^{-3}	777.8 × 10^{-3}
AC600-3h-1r	5.341	3.673	121.9 × 10^{-3}	380 × 10^{-3}

The intermediate sample AC550-3h-0.5r shows a moderate Rs (3.818 Ω) and Rct (8.321 Ω), with a comparable Warburg factor (B = 777.8 × 10^{-3} $s^{1/2}$) implying partially restricted ion mobility due to less interconnected pores. In contrast, AC550-2h-1r exhibits a similar Rs (2.041 Ω) but the highest Rct (21.51 Ω), revealing increased charge transfer

resistance likely caused by insufficient pore connectivity or residual surface functionalities limiting electrolyte access. The slightly higher Rs observed for AC600-3h-1r (5.341 Ω) compared to its counterparts may stem from thicker electrode films, non-uniform binder distribution, or minor contact resistance within the test cell; however, this does not significantly compromise its overall electrochemical behavior as confirmed by its low Rct and robust capacitance retention (see Section 4.2.3). Notably, these values are consistent with literature benchmarks for biomass-derived porous carbons; for example, a recent study on rice straw biochar electrodes reported Rs values between 0.4 and 0.7 Ω and Rct in the range of 3-5 Ω under similar test configurations.[45] The detailed fitted ECM parameters for all samples are summarized in Table 6 for clarity.

4.2.3. Galvanostatic Charge Discharge (GCD) Analysis

Analysis of the galvanostatic charge–discharge (GCD) behaviors, integrated with normalized specific capacitance, energy density, power density, rate capability, and cyclic stability results, demonstrates the clear impact of synthesis conditions on the electrochemical performance of the hemp stem-derived activated carbons.

For the sample AC500-2h-0.5r, the GCD profiles recorded in both the 0-0.8 V (Figure 14) and 0-1 V (Figure 15) potential windows indicate a moderate IR drop of approximately 0.02 to 0.025 V observed at the start of the discharge segment, which reflects the limited electrical conductivity of the carbon framework resulting from the relatively low activation temperature and reduced $ZnCl_2$ impregnation ratio (see Section 4.3.2). The discharge profiles within both voltage ranges maintain a linear character yet show a distinctly steeper slope compared to samples synthesized at higher temperatures or with a higher $ZnCl_2$ content, clearly demonstrating the lower specific capacitance that is confirmed numerically. The absence of bending or curvature in the discharge slope confirms that the charge storage occurs entirely through an electric double-layer mechanism without a significant faradaic contribution, while the short effective discharge duration in the plot indicates a limited ion-accessible surface area. When the upper potential limit is extended to 1V, the discharge path lengthens in a straight manner without the appearance of any new inflection or deviation, showing that the additional stored charge results only from the wider voltage range rather than a change in the charge storage process, with a slight increase in the IR drop as expected due to the higher current flow.

In contrast, AC550-2h-1r demonstrates a clear improvement both in measured values and overall GCD behavior. The IR drop in its discharge curves is evidently smaller (around 0.015-0.02 V), and the discharge slope is more gradual and extends further compared to AC500-2h-0.5r. The discharge line remains perfectly linear throughout the process, confirming the dominance of electric double-layer capacitive behavior and showing that the increased $ZnCl_2$ ratio combined with a moderately higher temperature effectively produced a better-connected pore network. The absence of any deviation or bending at higher voltages further supports that no undesirable faradaic side reactions occur when the potential reaches 1 V in aqueous electrolyte.

Compared with AC550-3h-0.5r, which was activated at the same temperature but with a longer duration, the GCD curves display an intermediate pattern. The IR drop is only slightly lower (about 0.015 V), but the discharge slope remains steeper than that of AC550-2h-1r, highlighting that extending the time alone cannot sufficiently open the pore structure if the amount of activating agent is limited. Increasing the window to 1 V results in a longer discharge region without any change in the slope trend, confirming stable double-layer charge storage but restricted capacity enhancement.

The effect of maximum thermal energy is most evident in AC600-1h-1r, which combines a high activation temperature with a short processing time. In its GCD profiles, the initial IR drop appears slightly higher than that of AC550-2h-1r (approximately 0.02-0.023 V), suggesting that some residual structural resistance remains due to the limited activation time, despite improved carbon ordering at elevated temperatures. The nearly linear slope confirms stable and uniform charge–discharge reversibility, with no signs of bending, sharp slope changes, or plateau regions, which validates a clean electric double-layer capacitance response. Extending the potential window to 1 V produces the same linear extension in the discharge curve, with the IR drop staying within an acceptable range and no evidence of electrolyte decomposition. For AC600-3h-1r, the initial IR drop is the lowest among all tested samples (around 0.018-0.019 V), demonstrating that the conductive pathways are well developed and free from excess residual activating agent or structural defects. The GCD profile of this sample remains fully linear and uniform, without any noticeable bending, inflection, or plateau, confirming that the charge storage mechanism is governed purely by electric double-layer behavior. Beyond this qualitative interpretation of the GCD curves, it is crucial to examine the quantitative performance indicators such as specific capacitance, the influence of the operating voltage, the

resulting energy and power densities, and the cycling durability to comprehensively evaluate the practical suitability of these hemp stem-derived activated carbons as electrode materials.

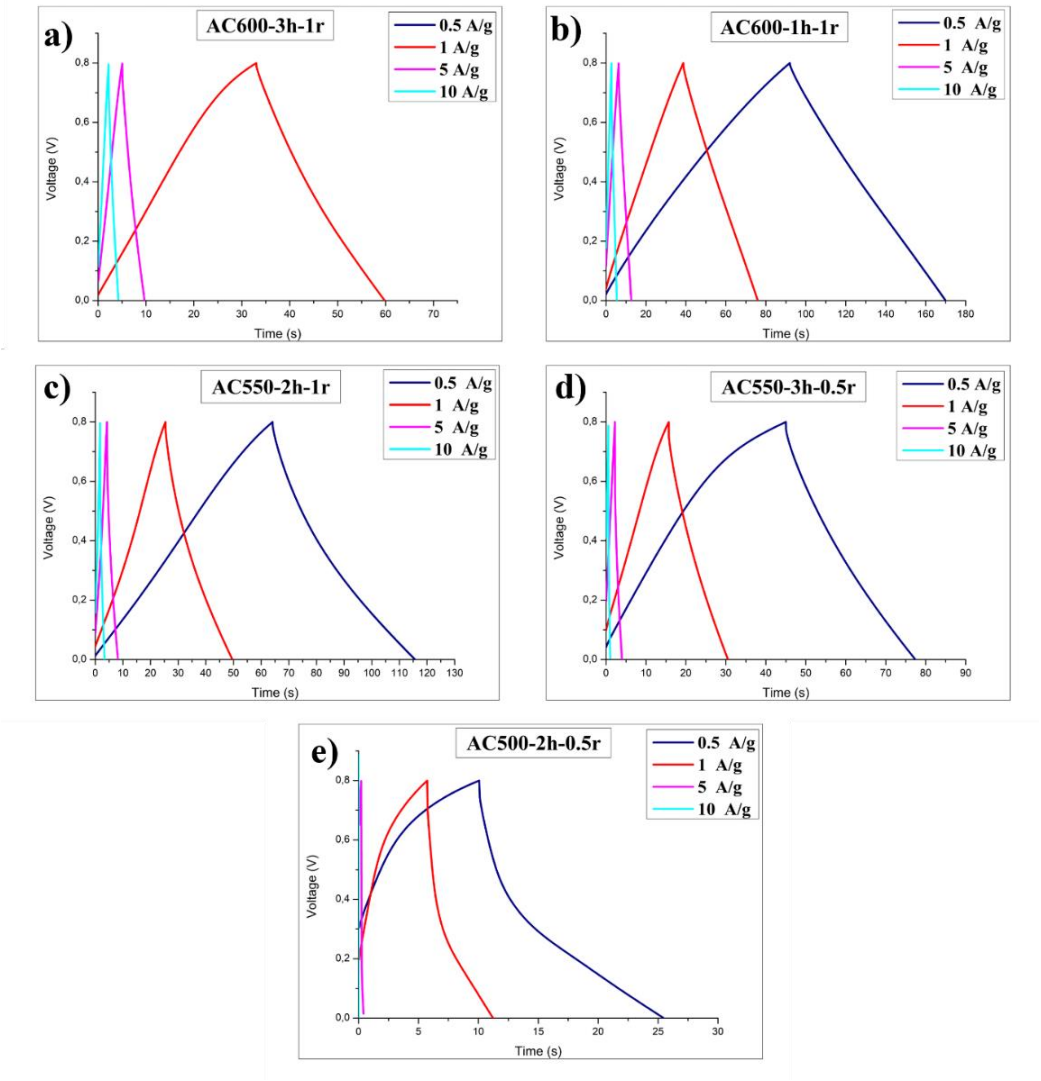

Figure 14. Galvanostatic charge–discharge (GCD) profiles of the selected hemp-derived activated carbon electrodes at various current densities (0.5, 1, 5, and 10 A/g) within a 0-0.8 V operating window

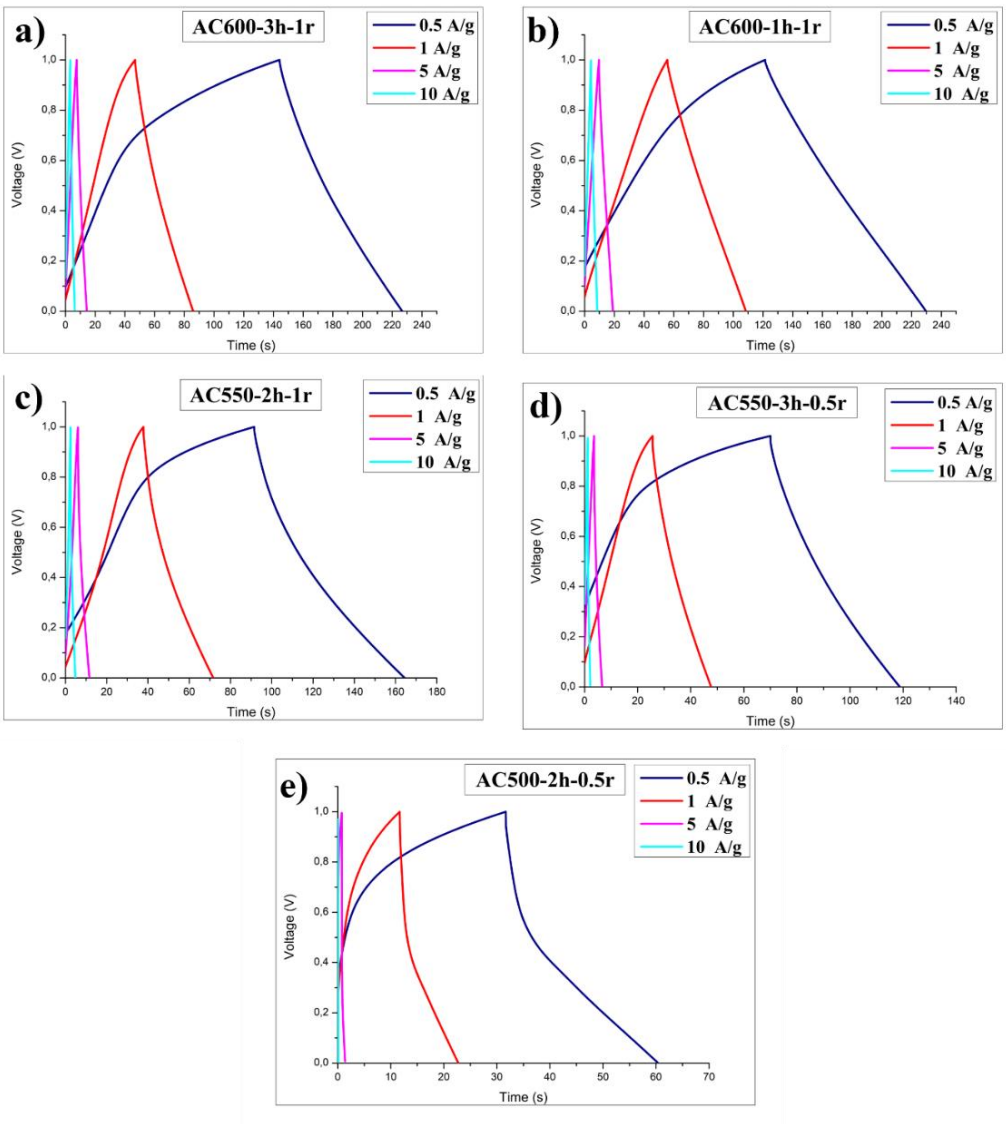

Figure 15. Galvanostatic charge–discharge (GCD) profiles of the selected hemp-derived activated carbon electrodes at various current densities (0.5, 1, 5, and 10 A/g) within a 0-1.0 V operating window

The quantitative electrochemical results offer a clear basis for understanding how the combined influence of carbonization temperature, activation time, and $ZnCl_2$ impregnation ratio governs the performance of the hemp stem-derived activated carbon electrodes. As presented in Table 7, within the 0–0.8 V working range, the highest specific capacitance values are observed for AC600-1h-1r and AC600-3h-1r, reaching 59.0 F/g and 58.1 F/g respectively at a current density of 0.5 A/g. These values decline gradually as the current density increases, dropping to 45.9 F/g and 34.0 F/g at 5 A/g, which confirms that the well-developed pore networks in these samples maintain relatively efficient ion transport even under faster charge–discharge conditions. In comparison, AC500-2h-0.5r, produced under the lowest temperature and with the lowest amount of activating agent, records the lowest specific capacitance, beginning at 23.4 F/g at 0.5 A/g and decreasing to below 10 F/g at 5 A/g, clearly indicating a severely restricted ion-accessible surface area.

Table 7. Electrochemical performance parameters at different current densities within 0-0.8V

	Specific Capacitance (F/g)			**Energy Density (Wh/kg)**			**Power Density (W/kg)**		
Electrode Material	**0.5 A/g**	**1A/g**	**5 A/g**	**0.5 A/g**	**1A/g**	**5 A/g**	**0.5 A/g**	**1A/g**	**5 A/g**
AC600-3h-1r	58.1	42.2	34.0	5.08	3.65	2.61	321.7	490.7	2042.2
AC600-1h-1r	59.0	50.9	45.9	5.17	4.40	3.56	239.3	426.3	2060.7
AC550-2h-1r	40.7	33.6	29.3	3.50	2.78	1.91	244.3	414.1	1768.7
AC550-3h-0.5r	29.7	22.4	17.8	2.47	1.74	0.78	274.7	424.4	1630.0
AC500-2h-0.5r	23.4	16.0	9.54	0.78	0.63	0.02	182.2	419.7	540.7

The effect of extending the operating voltage window is clearly demonstrated in Table 8. When the upper limit is increased to 1.0 V, the specific capacitance for AC600-3h-1r rises markedly to 79.5 F/g at 0.5 A/g, while AC600-1h-1r reaches 73.3 F/g under

the same conditions. This confirms that a wider potential range can significantly enhance charge storage within the electric double-layer mechanism by expanding the accessible energy region for ion adsorption. In parallel, the calculated energy densities almost double, as expected from their direct quadratic dependence on the operating voltage according to $E = \frac{1}{2} CV^2$. For AC600-3h-1r, the energy density increases from 5.08 Wh/kg at 0-0.8 V to 10.89 Wh/kg at 0-1 V at 0.5 A/g, and AC600-1h-1r shows a comparable improvement. Power density is also influenced by both the broader voltage range and the resulting discharge time; for AC600-3h-1r, the achievable power output increases from 321.7 W/kg at 0.8 V to 474.2 W/kg at 1 V at 0.5 A/g. This demonstrates that operating at higher voltage efficiently extends the usable energy window without triggering any undesirable faradaic side reactions, which is fully consistent with the linear GCD profiles and stable discharge behavior discussed in previous sections.

Table 8. Electrochemical performance parameters at different current densities within 0-1.0V

	Specific Capacitance (F/g)			**Energy Density (Wh/kg)**			**Power Density (W/kg)**		
Electrode Material	**0.5 A/g**	**1A/g**	**5 A/g**	**0.5 A/g**	**1A/g**	**5 A/g**	**0.5 A/g**	**1A/g**	**5 A/g**
AC600-3h-1r	79.5	49.1	40.7	10.89	6.64	6.29	474.2	612.7	3358.7
AC600-1h-1r	73.3	59.0	53.3	10.04	8.01	8.22	334.1	546.7	3178.8
AC550-2h-1r	55.4	39.5	33.0	7.49	5.22	5.81	370.1	556.3	3792.4
AC550-3h-0.5r	28.3	28.3	21.0	3.73	3.62	4.35	275.5	591.8	5219.3
AC500-2h-0.5r	23.4	16.0	9.5	2.90	1.84	7.03	364.0	603.1	4289.9

The capacity to maintain charge storage at higher current densities, expressed as capacity retention, is summarized in Table 9 for the 0–0.8 V potential window. Among the tested samples, AC600-1h-1r shows the highest retention, preserving approximately

77.9% of its initial capacitance when the current density increases from 0.5 A/g to 5 A/g. This result highlights the effectiveness of high-temperature activation combined with an optimal $ZnCl_2$ ratio in producing an interconnected microporous network that supports efficient ion transport under faster charge–discharge conditions. AC600-3h-1r demonstrates moderate retention of about 58.5%, whereas AC500-2h-0.5r drops to around 54%, indicating limited ion-accessible pathways and greater internal resistance during high-rate cycling. This trend aligns well with the slope characteristics and IR drop behavior observed in the corresponding GCD profiles.

Table 9. Specific capacitance values at different current densities and calculated capacity retention from 0.5 A/g to 5 A/g

Electrode Material	**0.5Ag**	**1 A/g**	**5 A/g**	**Capacity Retention (%)**
AC600-3h-1r	58.11	42.23	34.02	58.54
AC600-1h-1r	59.04	50.89	45.96	77.85
AC550-2h-1r	40.71	33.58	29.31	72.00
AC550-3h-0.5r	29.66	22.37	17.88	60.27
AC500-2h-0.5r	10.10	9.41	5.48	54.28

Long-term cyclic stability is presented in Figure 16, which demonstrates that after 5000 continuous cycles at 20 A/g, AC600-1h-1r retains approximately 78% of its initial capacitance, confirming its robust structural integrity under prolonged operation. AC600-3h-1r shows slightly lower stability with around 58% retention, while the weakest performer, AC500-2h-0.5r, decreases to about 54%, further emphasizing how incomplete pore development limits cycle life. The coulombic efficiency, illustrated in Figure 17, remains consistently high between 97% and 100% for all samples over extended cycling, confirming excellent charge–discharge reversibility that is characteristic of electric double-layer capcapacitors.

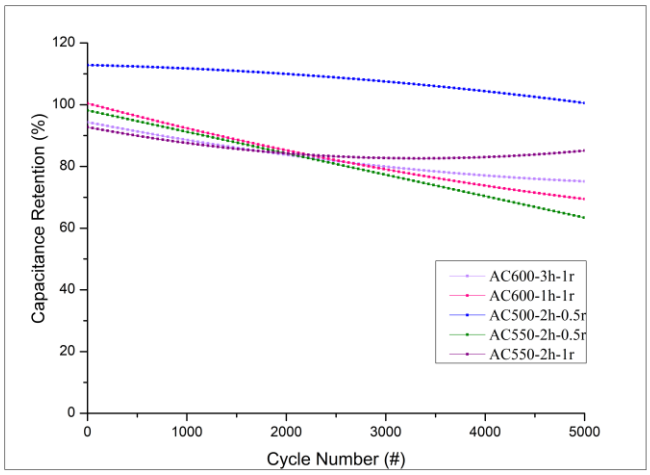

Figure 16. Capacitance retention of the electrodes over 5000 charge–discharge cycles at 20 A/g

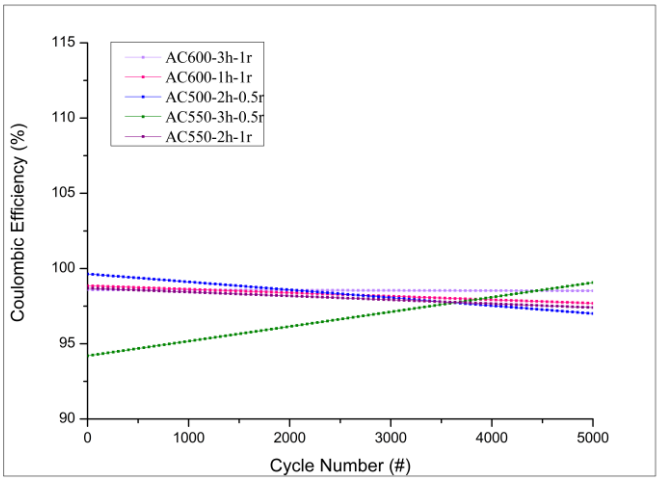

Figure 17. Coulombic efficiency profiles of the electrodes during long-term cycling at 20 A/g

4.3. Material Characterization

4.3.1. Nitrogen Adsorption Desorption Analysis

The nitrogen adsorption–desorption isotherms provide direct evidence of the porous structure formed under different activation conditions. As illustrated in Figure 18, all samples show steep nitrogen uptake at low relative pressures ($P/P_0 < 0.1$), confirming dominant microporosity—a typical feature of biomass-derived activated carbons.[46]

According to IUPAC classification, the isotherm for **AC500-2h-0.5r** demonstrates a classic **Type I** profile with a sharp knee and clear plateau, indicating that adsorption proceeds mainly through micropore filling via monolayer coverage. The lack of any significant hysteresis implies minimal mesopore development at this relatively low activation temperature and impregnation ratio.

In contrast, **AC550-2h-1r** retains the dominant Type I behavior but displays a clear **H_4-type hysteresis loop** at intermediate pressures ($P/P_0 \approx 0.4–0.9$). This indicates the coexistence of micropores with narrow slit-like mesopores, which promote partial capillary condensation an advantageous feature for enhancing ion transport.

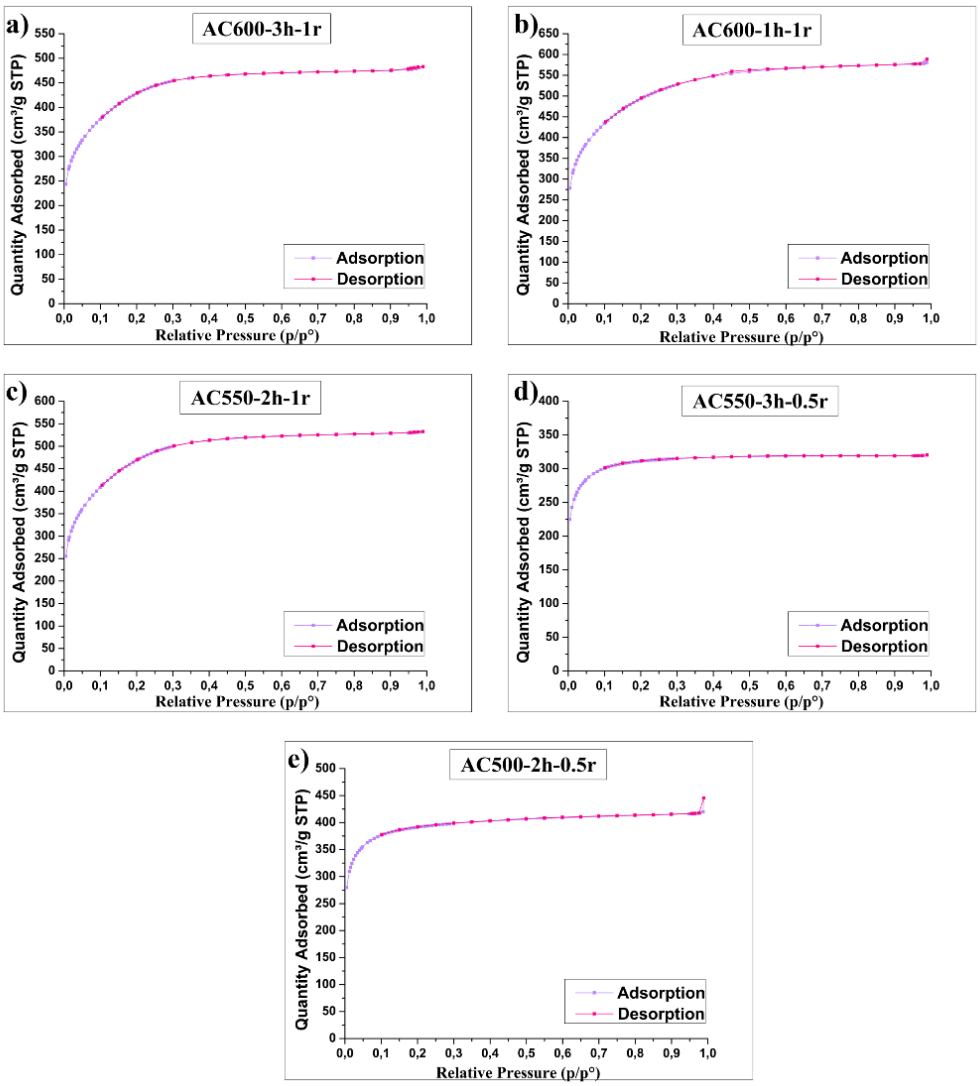

Figure 18. Nitrogen adsorption-desorption isotherms

For **AC550-3h-0.5r**, the isotherm again shows a strong microporous signature, with minimal hysteresis, suggesting that a longer activation time at a low $ZnCl_2$ ratio does not effectively generate mesopores and may even lead to partial pore shrinkage or collapse due to over-carbonization.[31] The isotherm of **AC600-1h-1r** combines high microporosity with visible mesoporosity, displaying a mixed **Type I/IV** pattern with a more defined hysteresis loop than AC550-2h-1r. The high temperature, moderate activation time, and sufficient chemical ratio synergistically promote a hierarchical pore network favorable for double-layer ion storage and rapid ion diffusion.[47] Finally, **AC600-3h-1r** shows a similar profile to AC600-1h-1r but with a broader hysteresis loop, implying further development of mesopores at the expense of micropore fraction due to prolonged activation. Such pore merging and widening are consistent with the known behavior of over-activated carbon materials.[46] In summary, the isotherm results confirm that micropore filling is the primary adsorption mechanism for all samples, while the controlled appearance of mesoporosity under higher temperature and optimal chemical conditions supports improved ion transport.

The pore size distribution (PSD) and BET surface area analyses provide deeper insight into how activation conditions fine-tune the balance between microporosity and mesoporosity, which directly influences the electrochemical behavior of carbon-based electrodes. As illustrated in Figure 19, all samples exhibit dominant microporous peaks centered near 1.1-1.3 nm, which confirms the effective development of narrow channels vital for high electric double-layer capacitance (EDLC). Such narrow micropores (<2 nm) contribute significantly to the total capacitance by providing abundant surface area for ion adsorption.[46]

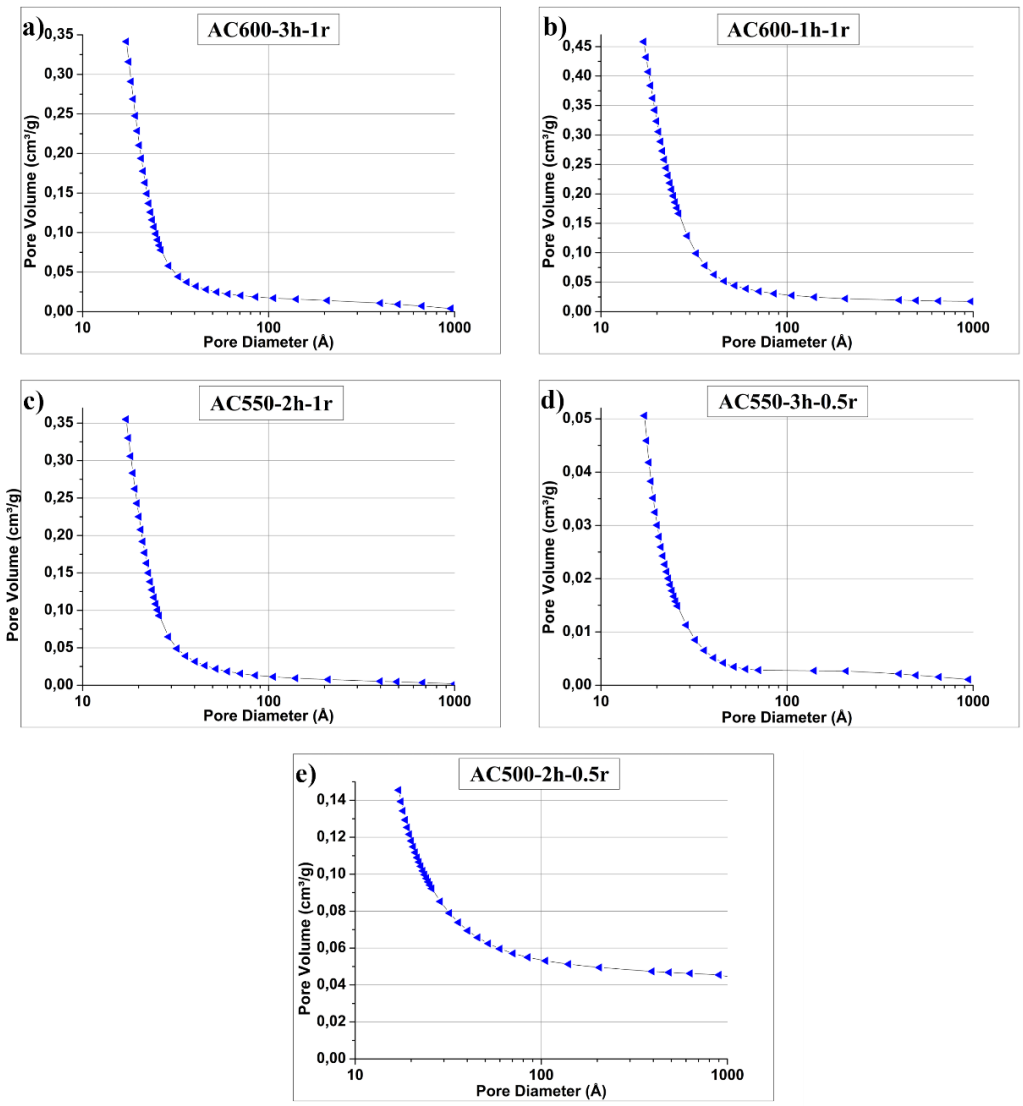

Figure 19. BJH pore size distribution curves

The impact of activation severity is clearly visible. Samples treated at lower temperatures and lower $ZnCl_2$ ratios, such as **AC500-2h-0.5r**, maintain a sharp and narrowly distributed micropore structure with almost no significant extension into the mesopore region. This narrow distribution ensures high capacitance at low current densities but may restrict ion mobility during high-rate charge–discharge operations due to limited ion transport pathways.[33] In contrast, **AC550-2h-1r** shows a slight but meaningful broadening of the pore size distribution into the mesopore range (~2–4 nm) due to the higher chemical impregnation ratio, demonstrating the enhanced chemical etching effect of $ZnCl_2$. This observation is consistent with the pore widening mechanism described by Rouquerol et al.[48], where activating agents penetrate carbon walls and open narrower pores into larger interconnected channels.

Among the tested conditions, **AC600-1h-1r** demonstrates the most favorable hierarchical structure by combining dominant microporosity with a well-defined mesoporous shoulder in the range of 2-5 nm. This bimodal pore system improves both charge storage and rate capability because mesopores serve as ion-buffering reservoirs and reduce ion diffusion resistance during rapid cycling.[33] Such hierarchical structures have repeatedly been shown to yield better rate performance and enhanced specific capacitance retention at high current densities compared to purely microporous carbon.[28]

Prolonged activation, as observed in **AC600-3h-1r**, further broadens the pore size distribution, indicating partial merging of micropores into larger mesopores due to extended etching and pore wall thinning.[31] While this promotes ion transport by shortening ion diffusion paths[9], excessive widening can reduce the total microporous surface area, thus slightly lowering the maximum capacitance achievable at low rates. Therefore, achieving an optimal balance between micropore volume and mesopore accessibility is crucial for ensuring high performance across a range of current densities.

The BET surface area results summarized in Table 10 reinforce these structural trends, showing that the highest surface area of **1808 m^2/g** for **AC600-1h-1r** is comparable to or even competitive with more complex multi-step activations reported in the literature, such as the 1949 m^2/g reported by Guo et al.[33] for dual KOH/NH_3 activation of hemp stem-derived carbon. Similarly, Bembenek et al.[31] highlight that tuning activation conditions can modulate the micro-mesopore ratio, which directly influences ion transport dynamics and capacitance retention.

In summary, the coexistence of high micropore content and well-developed mesopores in the best-performing samples demonstrates that the carefully adjusted $ZnCl_2$ activation successfully yields hierarchical porous carbons with excellent structural suitability for high-performance supercapacitor electrodes.

Table 10. BET surface area values

Sample	BET Surface Area (m^2/g)
AC600-3h-1r	1572.87
AC600-1h-1r	1808.36
AC550-2h-1r	1723.49
AC550-3h-0.5r	1191.55
AC500-2h-0.5r	1488.77

4.3.2. RAMAN

All five activated carbon samples exhibit the typical Raman spectral features of disordered carbon, characterized by a prominent D band near 1350 cm^{-1} and a G band around 1580–1600 cm^{-1} as shown in Figure 20. The G band corresponds to the in-plane vibrations of sp^2-bonded carbon atoms forming graphitic domains, while the D band originates from the breathing mode of sp^2 rings that become active due to structural defects or lattice disorder. The clear presence of both bands, with similar peak intensities, indicates that all samples contain a substantial degree of structural disorder, which is common for biomass-derived activated carbons. The positions of these bands are largely consistent across the different samples, showing only minor variations that suggest similar carbon bonding configurations, with slight changes possibly related to subtle differences in graphitic domain sizes or local strain.

The intensity ratio of the D and G bands (ID/IG) is a well-known indicator of the degree of structural order: a higher ratio implies a greater number of defects and hence a lower degree of graphitization, whereas a lower ratio suggests more extended graphitic domains and improved structural order. ID/IG values for all samples given in Table 11.

The ID/IG ratios provide clear insight into the structural ordering and defect density of the synthesized hemp stem-derived activated carbon samples. AC600-3h-1r

shows the highest disorder degree with an ID/IG of 0.96, followed by AC550-2h-1r (0.94) and AC550-3h-0.5r (0.92), while AC600-1h-1r exhibits a slightly lower ratio of 0.91. The lowest value is observed for AC500-2h-0.5r at 0.76, indicating a relatively higher degree of graphitization compared to the other samples. These values suggest that increased activation temperature and prolonged activation time generally promote defect generation due to more aggressive pore development, which aligns with reports in the literature for hemp-based carbons.[33,49,50].The relatively higher ID/IG ratio of AC600-3h-1r confirms that extended activation time at high temperatures leads to more edge sites and micropores, which is beneficial for enhancing ion-accessible surface area but may slightly reduce electrical conductivity due to the higher defect density. This trend is fully consistent with the BET surface area and pore volume results (see Section 4.3.1) and aligns well with the EIS-derived charge transfer resistances (see Section 4.2.2). Overall, the ID/IG findings demonstrate that tuning activation parameters allows for a balance between structural ordering and defect-induced active sites, which directly influences the electrochemical double-layer capacitance and cycling stability of the produced carbon electrodes.

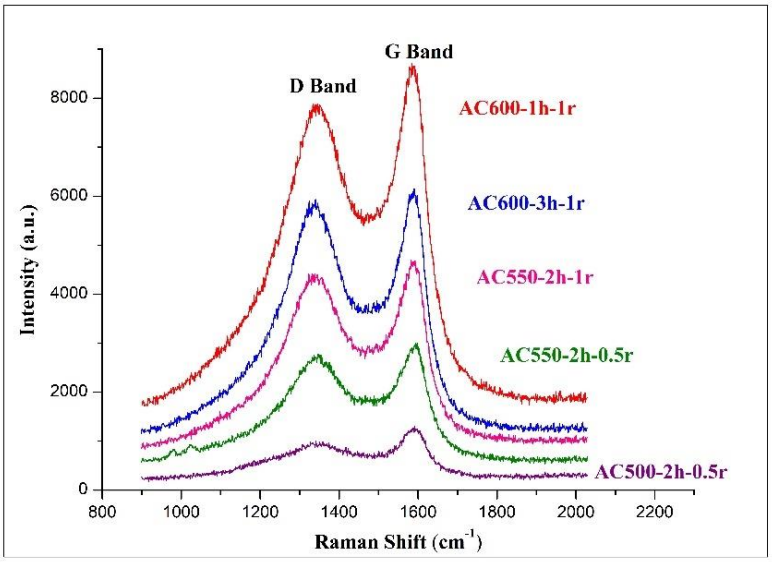

Figure 20. RAMAN spectrum of electrodes

Table 11. ID/IG values

Sample	ID/IG
AC600-3h-1r	0.96
AC600-1h-1r	0.91
AC550-2h-1r	0.94
AC550-3h-0.5r	0.92
AC500-2h-0.5r	0.76

4.3.3. SEM-EDX

The SEM images (Figure 21) clearly show that the surface morphology and pore structure of the activated carbon samples vary noticeably depending on the synthesis conditions. In general, all samples exhibit a porous, foam-like texture typical of $ZnCl_2$ chemical activation, but the extent of porosity and the preservation of the biomass structure differ with temperature, activation time, and $ZnCl_2$ ratio. At lower activation severity, such as in AC500-2h-0.5r, the carbon surface appears relatively dense and less porous, with only small pits indicating the initial formation of pores, so much of the original structure remains intact. As the activation becomes stronger, for example in AC550-2h-1r with a higher $ZnCl_2$ ratio, the carbon surface shows clear openings and channels where the activating agent has removed larger parts of the biomass matrix, creating a more connected network of micropores. At the highest severity, as in AC600-3h-1r, the structure becomes highly porous and more fragile, often showing thin carbon walls and cavities that give a skeletal, foam-like appearance under SEM. This trend is consistent with reports in the literature, where similar high-temperature activation has been shown to maintain or reshape the fibrous nature of biomass. For instance, studies on $ZnCl_2$-activated hemp or wood carbons note that while moderate conditions can preserve the original cell structure with added pores, harsher conditions can lead to visible cracks, exfoliated layers, or a porous network where the original shape is almost lost. Likewise, Gunasekaran et al. described that longer activation durations can transform a compact carbon matrix into an interconnected network with larger visible voids and macropores, confirming that extended chemical activation deepens pore development but also weakens the framework. This explains why in our series, AC550-3h-0.5r likely retains more of the precursor's cell walls, while AC600-1h-1r and AC600-3h-1r show more structural collapse due to higher temperature, longer time, and increased $ZnCl_2$ loading. Overall, SEM analysis confirms that stronger activation leads to more developed porosity and rougher surfaces, which is desirable for applications that benefit from high surface area. However, as also seen in the literature, too aggressive activation may reduce mechanical integrity, producing fragile, powdery carbons rather than stable granules. Therefore, the balance between pore creation and structural stability must be carefully adjusted to achieve a carbon material that combines high porosity with sufficient durability for practical use.

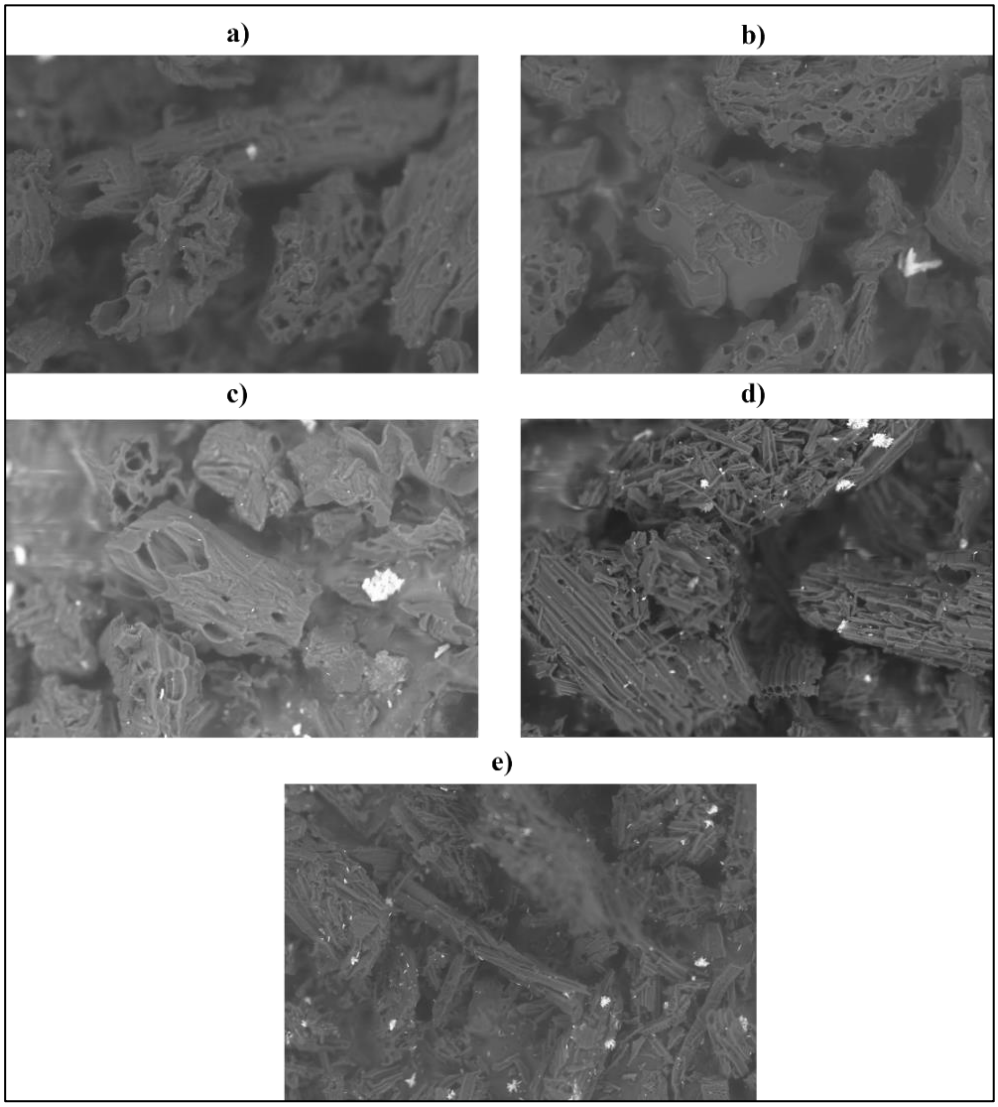

Figure 21. SEM images of theelectrodes (a) AC600-3h-1r, (b) AC600-1h-1r, (c) AC550-2h-1r, (d) AC550-3h-0.5r, (e) AC500-2h-0.5r

The EDX analysis (Table 12) confirms that carbon is the dominant element in all samples, and its proportion increases with higher carbonization temperature and longer activation time, while the oxygen content decreases accordingly, indicating more complete removal of oxygen-containing surface groups as CO and CO_2 gases. This trend shows that harsher conditions yield more carbon-rich, deoxygenated structures, which matches the slight increase in graphitic ordering also seen in the Raman results. Interestingly, the nitrogen content varies considerably: while mild conditions lead to substantial nitrogen loss, higher temperature and longer activation appear to retain or even concentrate nitrogen in the carbon matrix, likely because the remaining mass becomes relatively richer in less-volatile heteroatoms. The detected nitrogen could originate from the biomass itself or from uptake during pyrolysis in an inert atmosphere, which may help improve surface properties such as wettability and pseudocapacitance. In addition, residual zinc is found in all samples due to incomplete removal of $ZnCl_2$ used as the chemical activator; most of this zinc likely remains as ZnO or bonded forms within the porous carbon, while chlorine is present only in small amounts, indicating that most of it was volatilized or removed by washing. This residual Zn might have contributed to the partial graphitization by catalyzing carbon rearrangement during pyrolysis, although excess zinc or chlorine should ideally be eliminated by acid washing to improve purity. Overall, the EDX results align with the microstructural trends observed: more severe synthesis conditions lead to carbons with higher carbon content, lower oxygen, moderate nitrogen enrichment, and residual activator-derived species that slightly affect the final composition and properties.

Table 12. EDX elemental composition of electrodes

Sample	Element	Weight(%)	Atomic(%)
AC550-2h-1r	C	60.39	70.55
	N	9.07	8.70
	O	21.77	18.71
	P	0.03	0.01
	S	0.11	0.05
	Cl	0.08	0.03
	Zn	8.54	1.95
AC550-3h-0.5r	C	68.73	77.09
	N	6.94	6.59
	O	17.37	14.55
	P	0.10	0.04
	S	0.21	0.08
	Cl	1.45	0.55
	Zn	5.22	1.10
AC600-3h-1r	C	64.80	73.25
	N	12.58	12.11
	O	15.25	12.95
	P	0.04	0.02

(cont. on next page)

Table 12. (cont.)

	S	0.13	0.07
	Cl	0.57	0.22
	Zn	6.63	1.40
AC600-1h-1r	C	63.31	70.98
	N	14.77	14.22
	O	16.04	13.50
	P	0.11	0.04
	S	0.13	0.27
	Cl	0.22	0.08
	Zn	5.42	1.12
AC500-2h-0.5r	C	63.39	73.00
	N	11.93	11.77
	O	15.20	13.14
	P	0.05	0.02
	S	0.09	0.04
	Cl	0.26	0.10
	Zn	9.14	1.94

4.3.4. FTIR

Comparative analysis of the FTIR spectra reveals how the surface properties of the five activated carbon samples respond to varying activation conditions involving different temperatures, durations, and $ZnCl_2$/biomass ratios (Figure 22). The broad band observed in all samples in the range of approximately 3400–3600 cm^{-1} indicates the presence of hydroxyl groups or adsorbed water on the activated carbon surface. This band is particularly prominent in the AC500-2h-0.5r sample and gradually weakens with increasing temperature and duration. This trend suggests that higher temperature and longer activation time contribute to the removal of –OH groups and moisture from the surface (Lua & Yang, 2004).[51]

Similarly, the sharp peak observed around 1700–1750 cm^{-1} corresponds to carbonyl groups (carboxylic, ester, or ketone functionalities). This peak appears more pronounced in the AC550-2h-1r sample, which was produced at a moderate temperature (550 °C) with a relatively higher $ZnCl_2$ ratio, implying that $ZnCl_2$ activation may help preserve certain oxygen-containing surface groups. However, when the temperature is increased to 600 °C and the duration extended to 3 hours, the intensity of this peak decreases significantly, as seen in the AC600-3h-1r sample. This indicates that elevated temperature and extended duration promote the decomposition of oxygen-containing surface groups, leading to a more hydrophobic carbon surface.[52]

The band in the range of approximately 1500-1600 cm^{-1}, which represents aromatic C=C bonds, is present in all samples and becomes sharper and more distinct as the carbonization temperature and activation duration increase. The clearer presence of this band in the AC600 series demonstrates that higher temperatures favor the development of graphitic structures, which is further supported by the higher ID/IG ratios obtained from the Raman analysis (see section 4.3.2), confirming increased structural ordering and aromatic domain growth.

Additionally, bands identified within the 1000–1300 cm^{-1} range are more pronounced in samples produced at moderate temperatures with a suitable $ZnCl_2$ ratio (e.g., AC550-2h-1r), indicating the presence of C–O bonds (such as alcohols, ethers, or phenolic groups) on the surface. It is believed that $ZnCl_2$, through its dehydration and cross-linking effects, may stabilize certain oxygen-containing surface functionalities.[52]

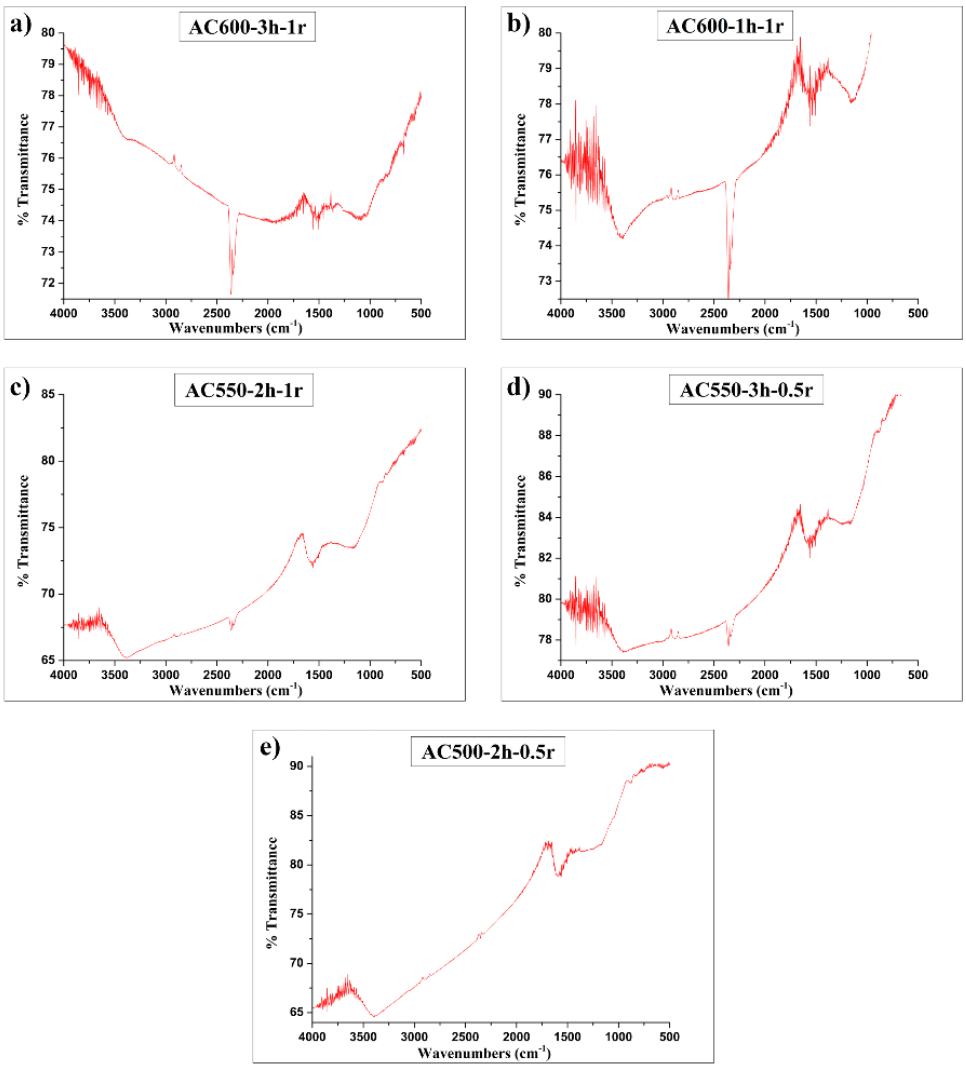

Figure 22. FTIR spectra

4.4. Comparison of Results

The comprehensive comparison of the experimental findings clearly demonstrates how the systematically varied synthesis parameters namely, carbonization temperature, activation duration, and $ZnCl_2$ impregnation ratio jointly define the physicochemical properties and electrochemical behavior of the hemp stem-derived activated carbons. The electrochemical analyses, including CV, GCD, and EIS tests, consistently show that samples activated at higher temperatures with optimized chemical ratios and suitable activation times (e.g., AC600-1h-1r and AC600-3h-1r) deliver superior specific capacitance, enhanced energy and power densities, and robust cycle life compared to those produced under milder conditions (e.g., AC500-2h-0.5r). This trend directly correlates with the well-developed hierarchical porosity confirmed by the BET surface area and pore size distribution data (see Section 4.3.1), which highlight that increased micropore and mesopore coexistence supports efficient ion transport and storage, especially under high current densities.

Likewise, the Raman analysis (Section 4.3.2) indicates that higher activation temperatures and prolonged activation times lead to slightly increased defect densities, as evidenced by higher ID/IG ratios. While these structural defects can marginally reduce electrical conductivity, they also generate more active sites, improving the double-layer capacitance, a trend that aligns with the improved charge transfer resistance observed in the EIS profiles (Section 4.2.2). SEM images further reinforce this synergy by illustrating that high-performing samples exhibit a more open, foam-like texture with extensive pore connectivity, whereas low-performing carbons retain denser, less permeable structures that hinder ion accessibility (Section 4.3.3).

The elemental composition data derived from EDX analysis (Section 4.3.3) show that samples synthesized under harsher conditions have higher carbon content and reduced oxygen and chlorine residues, pointing to more complete carbonization and effective post-treatment. The presence of residual nitrogen and traces of zinc further suggests potential pseudocapacitive contributions and partial catalytic graphitization, which complement the primary electric double-layer storage mechanism.

Collectively, these results confirm that tailoring the activation parameters enables fine control over pore development, surface functionality, and structural ordering, which together govern ion transport dynamics and charge storage efficiency. The consistent

agreement among the electrochemical tests, structural analyses, and surface chemistry demonstrates that the carefully tuned $ZnCl_2$ chemical activation strategy applied to hemp stems successfully produces high-performance carbon electrodes suitable for practical supercapacitor applications.

CHAPTER 5

CONCLUSION

This thesis investigated the production of activated carbon from hemp stems and its application as electrode material for supercapacitors. A response-surface Box–Behnken experimental design was used to optimize the key activation parameters that activation temperature, activation time, and $ZnCl_2$/biomass ratio. The hemp stem-based activated carbons were characterized in terms of their physicochemical properties and electrochemical performance. The main findings indicated that careful control of the activation conditions can yield a carbon material with very high surface area and a tailored pore structure, resulting in superior capacitive performance.

Experimental design model indicated that an activation temperature of 600 °C, an activation time of 1 hour, and an impregnation ratio of 1.2 represent the optimal conditions for simultaneously maximizing specific capacitance and energy density.

The best-performing samples produced within the experimental matrix achieved a specific surface area 1880 m^2/g with a hierarchical pore network of abundant micropores and accessible mesopores. Raman spectroscopy confirmed moderate structural disorder (ID/IG up to 0.96), providing a balance between defect sites and graphitic domains. Electrochemical tests showed that these features resulted in excellent capacitor performance: the optimized electrodes achieved a specific capacitance of up to 79.5 F/g at 0.5 A/g in a 0–1 V window and retained about 78% of their initial capacitance after 5000 cycles at 20 A/g, while maintaining coulombic efficiency above 97%. Expanding the operating voltage range from 0–0.8 V to 0–1 V nearly doubled the energy density, demonstrating that the well-developed pore structure supports efficient ion transport and stable charge storage.

Overall, these findings demonstrate that hemp stems can be transformed into sustainable, cost-effective electrode materials for practical supercapacitor applications when combined with carefully controlled chemical activation. Future work should

explore scaling up the process, integrating hybrid materials, and assembling full-cell devices to realize the full potential of biomass-based energy storage solutions.

REFERENCES

1. Olabi, A. G.; Abbas, Q.; Al Makky, A.; Abdelkareem, M. A. Supercapacitors as next Generation Energy Storage Devices: Properties and Applications. *Energy* **2022**, *248*, 123617. https://doi.org/10.1016/J.ENERGY.2022.123617.
2. Zhu, S.; Guan, C.; Wu, Y.; Ni, J.; Han, G. Upgraded Structure and Application of Coal-Based Graphitic Carbons Through Flash Joule Heating. *Adv Funct Mater* **2024**, *34* (39). https://doi.org/10.1002/ADFM.202403961.
3. Ponzio, R. A.; Coneo-Rodríguez, R.; Mondino, T. M.; Moreno, M. S.; Planes, G. Á. Ultraviolet Light–Assisted Synthesis of Nanostructured Carbon Materials for Supercapacitor Electrodes by Using Zinc Oxide Structures as Template and Catalyst. *Journal of Solid State Electrochemistry* **2024**, *28* (7), 2081–2091. https://doi.org/10.1007/S10008-023-05740-2.
4. Talaat, M.; Farahat, M. A.; Elkholy, M. H. Renewable Power Integration: Experimental and Simulation Study to Investigate the Ability of Integrating Wave, Solar and Wind Energies. *Energy* **2019**, *170*, 668–682. https://doi.org/10.1016/J.ENERGY.2018.12.171.
5. Shuja, A.; Khan, H. R.; Murtaza, I.; Ashraf, S.; Abid, Y.; Farid, F.; Sajid, F. Supercapacitors for Energy Storage Applications: Materials, Devices and Future Directions: A Comprehensive Review. *Journal of Alloys and Compounds*. Elsevier Ltd December 25, **2024**. https://doi.org/10.1016/j.jallcom.2024.176924.
6. Zhang, J.; Gu, M.; Chen, X. Supercapacitors for Renewable Energy Applications: A Review. *Micro and Nano Engineering* **2023**, *21*. https://doi.org/10.1016/j.mne.2023.100229.
7. Pandolfo, A. G.; Hollenkamp, A. F. Carbon Properties and Their Role in Supercapacitors. *J Power Sources* **2006**, *157* (1), 11–27. https://doi.org/10.1016/J.JPOWSOUR.2006.02.065.
8. Subramaniam, T.; Nainar, M. A. M.; Nordin, N. A. A Review on Synthesis and Characterization of Activated Carbon from Natural Fibers for Supercapacitor Application. *Pertanika Journal of Science and Technology*. Universiti Putra Malaysia Press January 1, **2022**, pp 351–376. https://doi.org/10.47836/pjst.30.1.20.

9. Simon, P.; Gogotsi, Y. Materials for Electrochemical Capacitors. *Nature Materials*. November 16, **2008**, pp 845–854. https://doi.org/10.1038/nmat2297.
10. Reenu; Sonia; Phor, L.; Kumar, A.; Chahal, S. Electrode Materials for Supercapacitors: A Comprehensive Review of Advancements and Performance. *Journal of Energy Storage*. Elsevier Ltd April 20, **2024**. https://doi.org/10.1016/j.est.2024.110698.
11. Firmansyah, D. A Review: Exploring Carbon Electrode Structures and Electrochemical Parameters to Enhance Supercapacitor Performance. *Analytical and Bioanalytical Electrochemistry*. Center of Excellence in Electrochemistry, Univ. of Tehran May 1, **2024**, pp 459–472. https://doi.org/10.22034/abec.2024.713504.
12. Luo, L.; Lan, Y.; Zhang, Q.; Deng, J.; Luo, L.; Zeng, Q.; Gao, H.; Zhao, W. A Review on Biomass-Derived Activated Carbon as Electrode Materials for Energy Storage Supercapacitors. *Journal of Energy Storage*. Elsevier Ltd November 30, **2022**. https://doi.org/10.1016/j.est.2022.105839.
13. Singh, N.; Singh, V.; Bisht, N.; Negi, P.; Dhyani, A.; Sharma, R. K.; Tewari, B. S. A Comprehensive Review on Supercapacitors: Basics to Recent Advancements. *Journal of Energy Storage*. Elsevier Ltd June 15, **2025**. https://doi.org/10.1016/j.est.2025.116498.
14. Haider, R.; Sagadevan, S.; Cameron, N. R.; Johan, M. R. Biomass-Derived Activated Carbon for High-Performance Energy Storage Devices. *J Power Sources* **2025**, *633*, 236404. https://doi.org/10.1016/J.JPOWSOUR.2025.236404.
15. Zhang, M.; Zhang, J.; Ran, S.; Sun, W.; Zhu, Z. Biomass-Derived Sustainable Carbon Materials in Energy Conversion and Storage Applications: Status and Opportunities. A Mini Review. *Electrochemistry Communications*. Elsevier Inc. May 1, **2022**. https://doi.org/10.1016/j.elecom.2022.107283.
16. Wu, K. J.; Young, W. Bin; Young, C. Structural Supercapacitors: A Mini-Review of Their Fabrication, Mechanical & Electrochemical Properties. *J Energy Storage* **2023**, *72*, 108358. https://doi.org/10.1016/J.EST.2023.108358.
17. Libber, M.; Gariya, N.; Kumar, M. A Comprehensive Analysis of Supercapacitors with Current Limitations and Emerging Trends in Research. *Journal of Solid State Electrochemistry*. Springer Science and Business Media Deutschland GmbH **2024**. https://doi.org/10.1007/s10008-024-06107-x.

18. Mandal, S.; Hu, J.; Shi, S. Q. A Comprehensive Review of Hybrid Supercapacitor from Transition Metal and Industrial Crop Based Activated Carbon for Energy Storage Applications. *Mater Today Commun* **2023**, *34*, 105207. https://doi.org/10.1016/J.MTCOMM.2022.105207.
19. Shi, Z.; Yue, L.; Wang, X.; Lei, X.; Sun, T.; Li, Q.; Guo, H.; Yang, W. 3D Mesoporous Hemp-Activated Carbon/Ni3S2 in Preparation of a Binder-Free Ni Foam for a High Performance All-Solid-State Asymmetric Supercapacitor. *J Alloys Compd* **2019**, *791*, 665–673. https://doi.org/10.1016/j.jallcom.2019.03.259.
20. Wang, J.; Huo, T.; Zhao, Y.; Lu, R.; Wu, X. Recent Advances in Heteroatoms-Doped Porous Carbon Electrode Materials for Supercapacitors: A Review. *J Energy Storage* **2025**, *110*, 115216. https://doi.org/10.1016/J.EST.2024.115216.
21. Guan, L.; Li, D.; Ji, S.; Wei, X.; Meng, F. Structural Regulation and Performance Enhancement of Carbon-Based Supercapacitors: Insights into Electrode Material Engineering. *Materials **2025**, Vol. 18, Page 456* 2025, *18* (2), 456. https://doi.org/10.3390/MA18020456.
22. Lobato-Peralta, D. R.; Okoye, P. U.; Alegre, C. A Review on Carbon Materials for Electrochemical Energy Storage Applications: State of the Art, Implementation, and Synergy with Metallic Compounds for Supercapacitor and Battery Electrodes. *Journal of Power Sources*. Elsevier B.V. October 15, **2024**. https://doi.org/10.1016/j.jpowsour.2024.235140.
23. Dissanayake, K.; Kularatna-Abeywardana, D. A Review of Supercapacitors: Materials, Technology, Challenges, and Renewable Energy Applications. *J Energy Storage* **2024**, *96*, 112563. https://doi.org/10.1016/J.EST.2024.112563.
24. Wang, G.; Zhang, L.; Zhang, J. A Review of Electrode Materials for Electrochemical Supercapacitors. *Chem Soc Rev* **2012**, *41* (2), 797–828. https://doi.org/10.1039/C1CS15060J.
25. Tan, Y.; Yang, C.; Qian, W.; Teng, C. Flower-like MnO2 on Layered Carbon Derived from Sisal Hemp for Asymmetric Supercapacitor with Enhanced Energy Density. *J Alloys Compd* **2020**, *826*. https://doi.org/10.1016/j.jallcom.2020.154133.
26. Sun, W.; Lipka, S. M.; Swartz, C.; Williams, D.; Yang, F. Hemp-Derived Activated Carbons for Supercapacitors. *Carbon N Y* **2016**, *103*, 181–192. https://doi.org/10.1016/j.carbon.2016.02.090.

27. Wang, Y.; Yang, R.; Li, M.; Zhao, Z. Hydrothermal Preparation of Highly Porous Carbon Spheres from Hemp (Cannabis Sativa L.) Stem Hemicellulose for Use in Energy-Related Applications. *Ind Crops Prod* **2015**, *65*, 216–226. https://doi.org/10.1016/j.indcrop.2014.12.008.
28. Tiwari, B.; Joshi, A.; Munjal, M.; Sharma, R. K.; Singh, G. A Heterojunction of VO(OH)2nanorods onto Hemp Stem Derived Carbon for High Voltage (1.5 V) Symmetric Supercapacitors. *Sustain Energy Fuels* **2020**, *4* (10), 5102–5113. https://doi.org/10.1039/d0se01038c.
29. Kotsyubynsky, V.; Rachiy, B.; Boychuk, V.; Budzulyak, I.; Turovska, L.; Hodlevska, M. Correlation between Structural Properties and Electrical Conductivity of Porous Carbon Derived from Hemp Bast Fiber. *Fullerenes Nanotubes and Carbon Nanostructures* **2022**, *30* (8), 873–882. https://doi.org/10.1080/1536383X.2022.2033729.
30. Gunasekaran, S. S.; Badhulika, S. High-Performance Solid-State Supercapacitor Based on Sustainable Synthesis of Meso-Macro Porous Carbon Derived from Hemp Fibres via CO2 Activation. *J Energy Storage* **2021**, *41*. https://doi.org/10.1016/j.est.2021.102997.
31. Bembenek, M.; Kotsyubynsky, V.; Boychuk, V.; Rachiy, B.; Budzulyak, I.; Kowalski, Ł.; Ropyak, L. Effect of Synthesis Conditions on Capacitive Properties of Porous Carbon Derived from Hemp Bast Fiber. *Energies (Basel)* **2022**, *15* (22). https://doi.org/10.3390/en15228761.
32. Wang, H.; Li, Z.; Mitlin, D. Tailoring Biomass-Derived Carbon Nanoarchitectures for High-Performance Supercapacitors. *ChemElectroChem* **2014**, *1* (2), 332–337. https://doi.org/10.1002/celc.201300127.
33. Guo, N.; Li, M.; Wang, Y.; Sun, X.; Wang, F.; Yang, R. N-Doped Hierarchical Porous Carbon Prepared by Simultaneous-Activation of KOH and NH3 for High Performance Supercapacitors. *RSC Adv* **2016**, *6* (103), 101372–101379. https://doi.org/10.1039/c6ra22426a.
34. Gao, Y.; Yue, Q.; Gao, B.; Li, A. Insight into Activated Carbon from Different Kinds of Chemical Activating Agents: A Review. *Science of The Total Environment* **2020**, *746*, 141094. https://doi.org/10.1016/J.SCITOTENV.2020.141094.
35. Bhat, S. A.; Kumar, V.; Kumar, S.; Atabani, A. E.; Anjum Badruddin, I.; Chae, K. J. Supercapacitors Production from Waste: A New Window for Sustainable Energy

and Waste Management. *Fuel* **2023**, *337*, 127125. https://doi.org/10.1016/J.FUEL.2022.127125.

36. Gunasekaran, S. S.; Badhulika, S. Divulging the Electrochemical Hydrogen Storage of Ternary BNP-Doped Carbon Derived from Biomass Scaled to a Pouch Cell Supercapacitor. *Int J Hydrogen Energy* **2021**, *46* (71), 35149–35160. https://doi.org/10.1016/j.ijhydene.2021.08.104.
37. Chaparro-Garnica, J.; Salinas-Torres, D.; Mostazo-López, M. J.; Morallón, E.; Cazorla-Amorós, D. Biomass Waste Conversion into Low-Cost Carbon-Based Materials for Supercapacitors: A Sustainable Approach for the Energy Scenario. *Journal of Electroanalytical Chemistry* **2021**, *880*. https://doi.org/10.1016/j.jelechem.2020.114899.
38. Shi, Z.; Yue, L.; Wang, X.; Lei, X.; Sun, T.; Li, Q.; Guo, H.; Yang, W. 3D Mesoporous Hemp-Activated Carbon/Ni3S2 in Preparation of a Binder-Free Ni Foam for a High Performance All-Solid-State Asymmetric Supercapacitor. *J Alloys Compd* **2019**, *791*, 665–673. https://doi.org/10.1016/j.jallcom.2019.03.259.
39. Jiang, X.; Shi, G.; Wang, G.; Mishra, P.; Du, J.; Zhang, Y. Fe 2 O 3 /Hemp Straw-Based Porous Carbon Composite for Supercapacitor Electrode Materials. https://doi.org/10.1007/s11581-020-03547-z/Published.
40. Ferreira, S. L. C.; Bruns, R. E.; Ferreira, H. S.; Matos, G. D.; David, J. M.; Brandão, G. C.; da Silva, E. G. P.; Portugal, L. A.; dos Reis, P. S.; Souza, A. S.; dos Santos, W. N. L. Box-Behnken Design: An Alternative for the Optimization of Analytical Methods. *Anal Chim Acta* **2007**, *597* (2), 179–186. https://doi.org/10.1016/J.ACA.2007.07.011,.
41. Arectout, A.; Boukhal, H.; Chham, E.; Chakir, E.; Piñero-García, F.; Azahra, M.; El Yaakoubi, H.; Laazouzi, K.; El Ghalbzouri, T.; Assalmi, M. Assessment of Dead Layers Thickness of an HPGe Detector after an Extended Operating Period Using Response Surface Methodology and Box–Behnken Design. *Radiation Detection Technology and Methods* **2023**, *7* (4), 599–610. https://doi.org/10.1007/s41605-023-00421-0.
42. Bezerra, M. A.; Santelli, R. E.; Oliveira, E. P.; Villar, L. S.; Escaleira, L. A. Response Surface Methodology (RSM) as a Tool for Optimization in Analytical Chemistry. *Talanta* **2008**, *76* (5), 965–977. https://doi.org/10.1016/J.TALANTA.2008.05.019.

43. Montgomery. Design and Analysis of Experiments Ninth Edition. *Arizona State University* **2017**, 640.

44. Myers, R. H.; Montgomery, D. C.; Anderson-Cook, C. M. Building Empirical Models. *Response Surface Methodology: Process and Product Optimization Using Designed Experiments* **2016**, 13–62.

45. Liu, W.; Mei, J.; Liu, G.; Kou, Q.; Yi, T.; Xiao, S. Nitrogen-Doped Hierarchical Porous Carbon from Wheat Straw for Supercapacitors. *ACS Sustain Chem Eng* **2018**, *6* (9), 11595–11605. https://doi.org/10.1021/ACSSUSCHEMENG.8B01798/SUPPL_FILE/SC8B01798_SI_001.PDF.

46. Thommes, M.; Kaneko, K.; Neimark, A. V.; Olivier, J. P.; Rodriguez-Reinoso, F.; Rouquerol, J.; Sing, K. S. W. Physisorption of Gases, with Special Reference to the Evaluation of Surface Area and Pore Size Distribution (IUPAC Technical Report). *Pure and Applied Chemistry* **2015**, *87* (9–10), 1051–1069. https://doi.org/10.1515/PAC-2014-1117.

47. Guo, N.; Li, M.; Wang, Y.; Sun, X.; Wang, F.; Yang, R. N-Doped Hierarchical Porous Carbon Prepared by Simultaneous-Activation of KOH and NH3 for High Performance Supercapacitors. *RSC Adv* **2016**, *6* (103), 101372–101379. https://doi.org/10.1039/c6ra22426a.

48. Rouquerol, J.; Avnir, D.; Fairbridge, C. W.; Everett, D. H.; Haynes, J. M.; Pernicone, N.; Ramsay, J. D. F.; Sing, K. S. W.; Unger, K. K. Recommendations for the Characterization of Porous Solids (Technical Report). *Pure and Applied Chemistry* **1994**, *66* (8), 1739–1758. https://doi.org/10.1351/PAC199466081739/MACHINEREADABLECITATION/RIS.

49. Wang, H.; Xu, Z.; Kohandehghan, A.; Li, Z.; Cui, K.; Tan, X.; Stephenson, T. J.; King'Ondu, C. K.; Holt, C. M. B.; Olsen, B. C.; Tak, J. K.; Harfield, D.; Anyia, A. O.; Mitlin, D. Interconnected Carbon Nanosheets Derived from Hemp for Ultrafast Supercapacitors with High Energy. *ACS Nano* **2013**, *7* (6), 5131–5141. https://doi.org/10.1021/nn400731g.

50. Jiang, X.; Shi, G.; Wang, G.; Mishra, P.; Liu, C.; Dong, Y.; Zhang, P.; Tian, H.; Liu, Y.; Wang, Z.; Zhang, Q.; Zhang, H. A Hydrothermal Carbonization Process for the Preparation of Activated Carbons from Hemp Straw: An Efficient Electrode

Material for Supercapacitor Application. *Ionics (Kiel)* **2019**, *25* (7), 3299–3307. https://doi.org/10.1007/s11581-019-02850-8.

51. Lua, A. C.; Yang, T. Effect of Activation Temperature on the Textural and Chemical Properties of Potassium Hydroxide Activated Carbon Prepared from Pistachio-Nut Shell. *J Colloid Interface Sci* **2004**, *274* (2), 594–601. https://doi.org/10.1016/J.JCIS.2003.10.001.

52. Liou, T. H. Development of Mesoporous Structure and High Adsorption Capacity of Biomass-Based Activated Carbon by Phosphoric Acid and Zinc Chloride Activation. *Chemical Engineering Journal* **2010**, *158* (2), 129–142. https://doi.org/10.1016/J.CEJ.2009.12.016.

APPENDICES

APPENDIX A

DESIGN OF EXPERIMENT RESULTS

Analysis of Variance

Source	DF	Adj SS	Adj MS	F-Value	P-Value
Model	9	2039,84	226,649	4,52	0,080
Linear	3	1123,96	374,652	7,47	0,041
Temperature (°C)	1	498,53	498,526	9,94	0,034
Duration (h)	1	86,80	86,804	1,73	0,259
Ratio (Chemical/Biomass)	1	538,63	538,625	10,73	0,031
Square	3	622,50	207,498	4,14	0,102
Temperature (°C)*Temperature (°C)	1	3,91	3,906	0,08	0,794
Duration (h)*Duration (h)	1	173,72	173,724	3,46	0,136
Ratio (Chemical/Biomass)*Ratio (Chemical/Biomass)	1	327,13	327,134	6,52	0,063
2-Way Interaction	3	293,39	97,797	1,95	0,264
Temperature (°C)*Duration (h)	1	1,59	1,586	0,03	0,868
Temperature (°C)*Ratio (Chemical/Biomass)	1	157,95	157,953	3,15	0,151
Duration (h)*Ratio (Chemical/Biomass)	1	133,85	133,853	2,67	0,178
Error	4	200,70	50,175		
Lack-of-Fit	3	200,65	66,884	1383,95	0,020
Pure Error	1	0,05	0,048		
Total	13	2240,54			

Figure 23. Specific capacitance ANOVA table

Analysis of Variance

Source	DF	Adj SS	Adj MS	F-Value	P-Value
Model	9	226,548	25,1720	5,09	0,066
Linear	3	140,571	46,8569	9,48	0,027
Temperature (°C)	1	91,147	91,1472	18,44	0,013
Duration (h)	1	12,755	12,7546	2,58	0,183
Ratio (Chemical/Biomass)	1	36,669	36,6687	7,42	0,053
Square	3	64,756	21,5853	4,37	0,094
Temperature (°C)*Temperature (°C)	1	1,928	1,9285	0,39	0,566
Duration (h)*Duration (h)	1	17,728	17,7278	3,59	0,131
Ratio (Chemical/Biomass)*Ratio (Chemical/Biomass)	1	33,398	33,3978	6,76	0,060
2-Way Interaction	3	21,222	7,0739	1,43	0,358
Temperature (°C)*Duration (h)	1	0,002	0,0017	0,00	0,986
Temperature (°C)*Ratio (Chemical/Biomass)	1	6,274	6,2744	1,27	0,323
Duration (h)*Ratio (Chemical/Biomass)	1	14,946	14,9456	3,02	0,157
Error	4	19,768	4,9421		
Lack-of-Fit	3	19,674	6,5581	69,75	0,088
Pure Error	1	0,094	0,0940		
Total	13	246,317			

Figure 24. Energy density ANOVA table

Analysis of Variance

Source	DF	Adj SS	Adj MS	F-Value	P-Value
Model	9	2621,06	291,23	1,42	0,392
Linear	3	2216,76	738,92	3,60	0,124
Temperature (°C)	1	1501,93	1501,93	7,31	0,054
Duration (h)	1	332,78	332,78	1,62	0,272
Ratio (Chemical/Biomass)	1	382,05	382,05	1,86	0,244
Square	3	221,16	73,72	0,36	0,787
Temperature (°C)*Temperature (°C)	1	184,15	184,15	0,90	0,397
Duration (h)*Duration (h)	1	71,16	71,16	0,35	0,588
Ratio (Chemical/Biomass)*Ratio (Chemical/Biomass)	1	28,27	28,27	0,14	0,729
2-Way Interaction	3	183,13	61,04	0,30	0,827
Temperature (°C)*Duration (h)	1	114,92	114,92	0,56	0,496
Temperature (°C)*Ratio (Chemical/Biomass)	1	33,55	33,55	0,16	0,707
Duration (h)*Ratio (Chemical/Biomass)	1	34,67	34,67	0,17	0,702
Error	4	821,93	205,48		
Lack-of-Fit	3	687,94	229,31	1,71	0,500
Pure Error	1	133,99	133,99		
Total	13	3442,99			

Figure 25. Power density ANOVA table

Analysis of Variance

Source	DF	Adj SS	Adj MS	F-Value	P-Value
Model	9	227143	25238,1	0,74	0,678
Linear	3	106232	35410,7	1,03	0,468
Temperature (°C)	1	85007	85006,7	2,48	0,190
Duration (h)	1	20804	20803,8	0,61	0,479
Ratio (Chemical/Biomass)	1	422	421,6	0,01	0,917
Square	3	73155	24384,9	0,71	0,594
Temperature (°C)*Temperature (°C)	1	8632	8632,1	0,25	0,642
Duration (h)*Duration (h)	1	46431	46431,2	1,36	0,309
Ratio (Chemical/Biomass)*Ratio (Chemical/Biomass)	1	3968	3967,6	0,12	0,751
2-Way Interaction	3	47756	15918,7	0,46	0,722
Temperature (°C)*Duration (h)	1	2138	2138,3	0,06	0,815
Temperature (°C)*Ratio (Chemical/Biomass)	1	11	11,3	0,00	0,986
Duration (h)*Ratio (Chemical/Biomass)	1	45607	45606,6	1,33	0,313
Error	4	137024	34256,0		
Lack-of-Fit	3	136900	45633,4	368,47	0,038
Pure Error	1	124	123,8		
Total	13	364167			

Figure 26. Capacity retention ANOVA table

APPENDIX B

ELECTROCHEMICAL TEST RESULTS

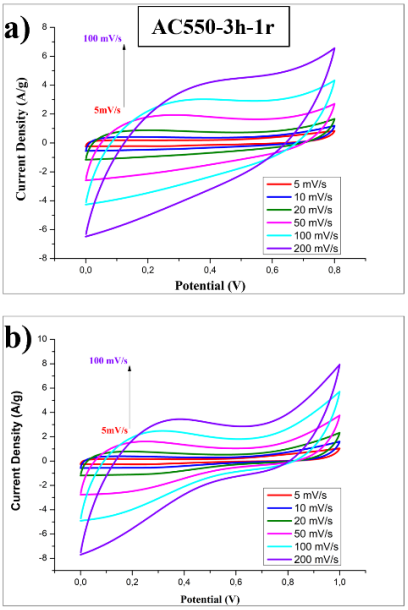

Figure 27. CV curves of AC550-3h-1r for a)0-0.8V and b)0-1.0V

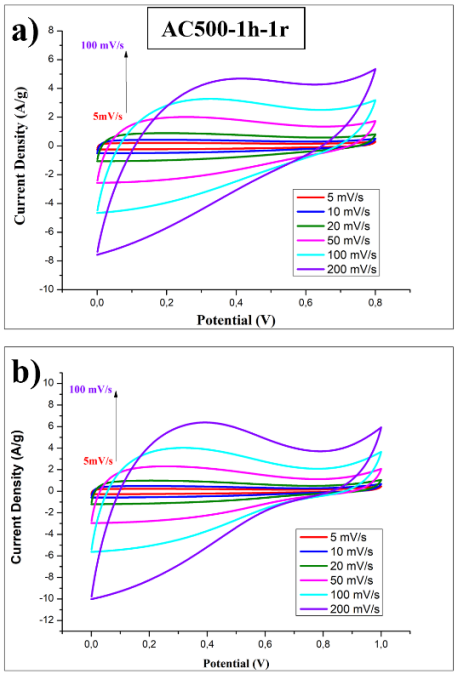

Figure 28. CV curves of AC500-1h-1r for a)0-0.8V and b)0-1.0V

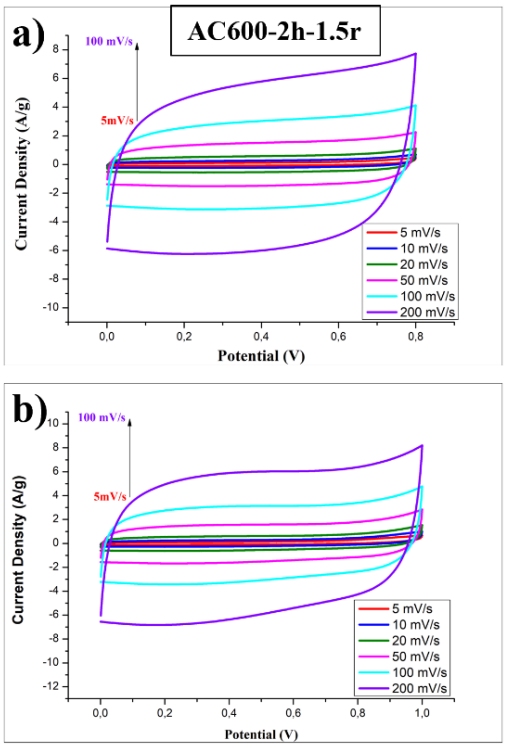

Figure 29. CV curves of AC600-2h-1.5r for a)0-0.8V and b)0-1.0V

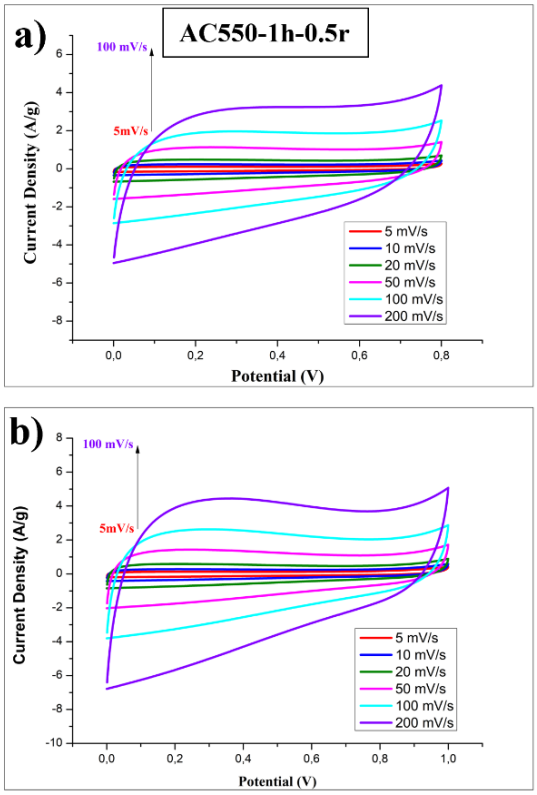

Figure 30. CV curves of AC600-2h-1.5r for a)0-0.8V and b)0-1.0V

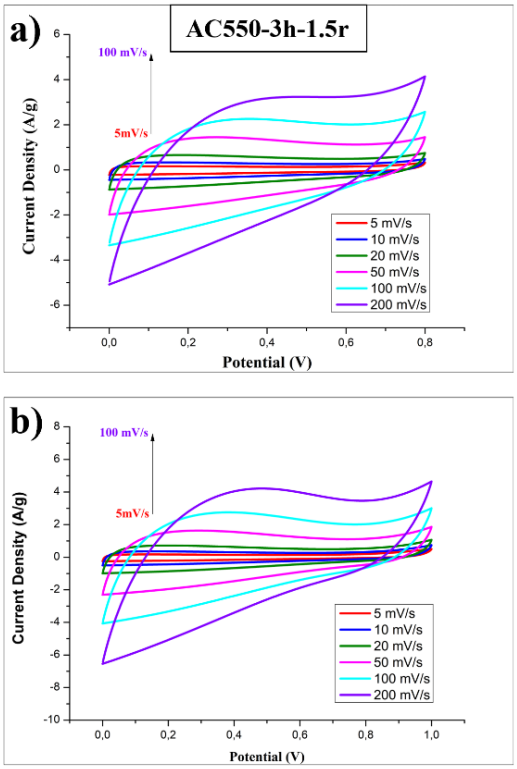

Figure 31. CV curves of AC550-3h-1.5r for a)0-0.8V and b)0-1.0V

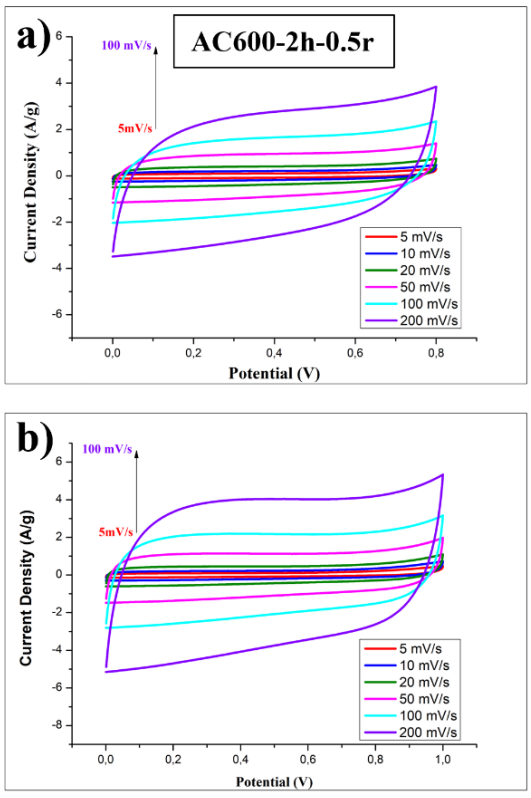

Figure 32. CV curves of AC600-2h-0.5r for a)0-0.8V and b)0-1.0V

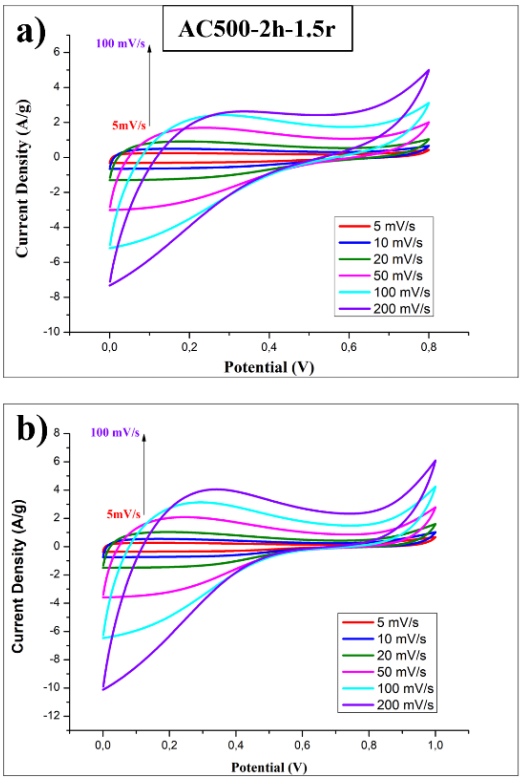

Figure 33. CV curves of AC500-2h-1.5r for a)0-0.8V and b)0-1.0V

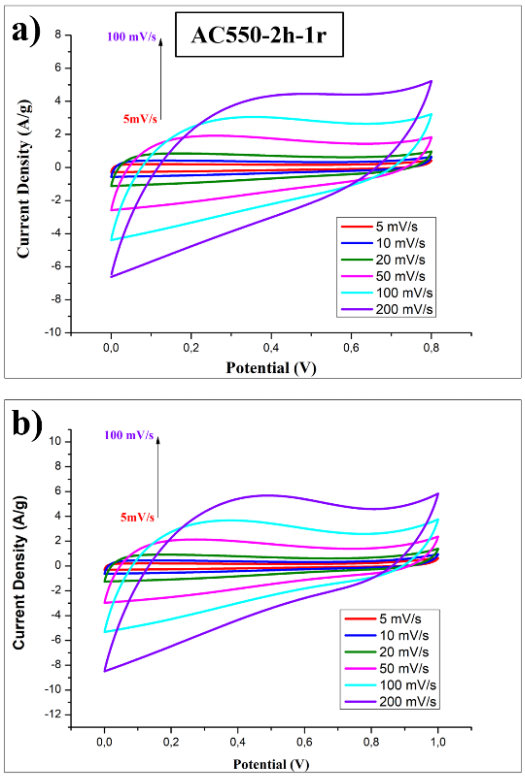

Figure 34. CV curves of AC550-2h-1r for a)0-0.8V and b)0-1.0V

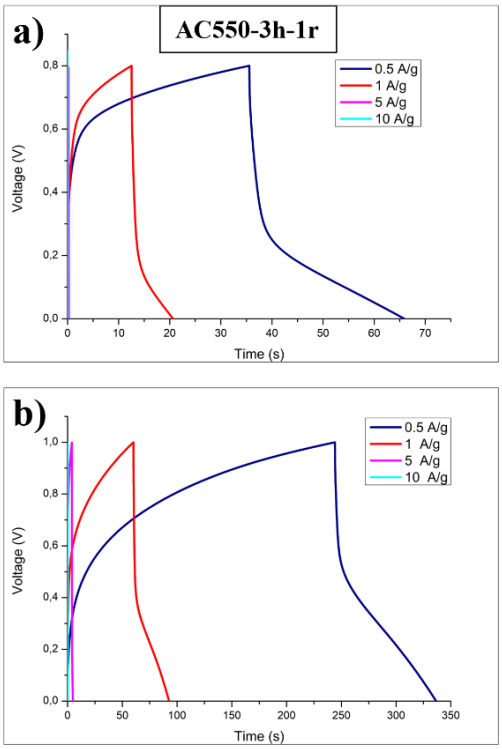

Figure 35. GCD curves of AC600-2h-1.5r for a)0-0.8V and b)0-1.0V

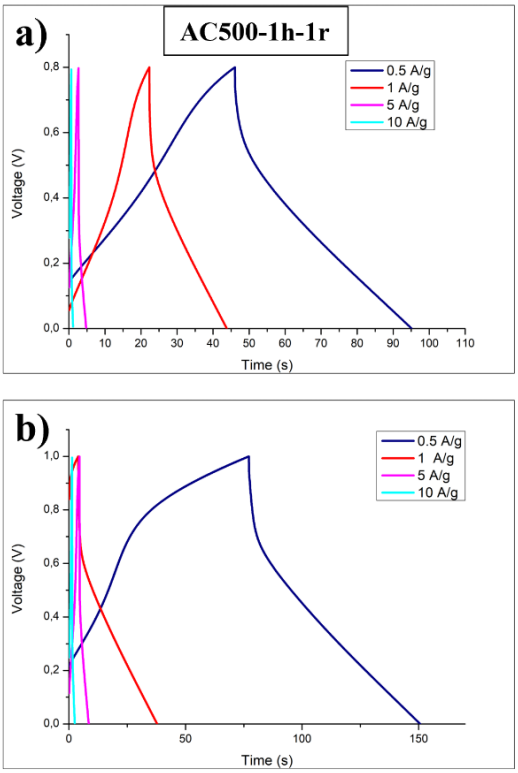

Figure 36. GCD curves of AC500-1h-1r for a)0-0.8V and b)0-1.0V

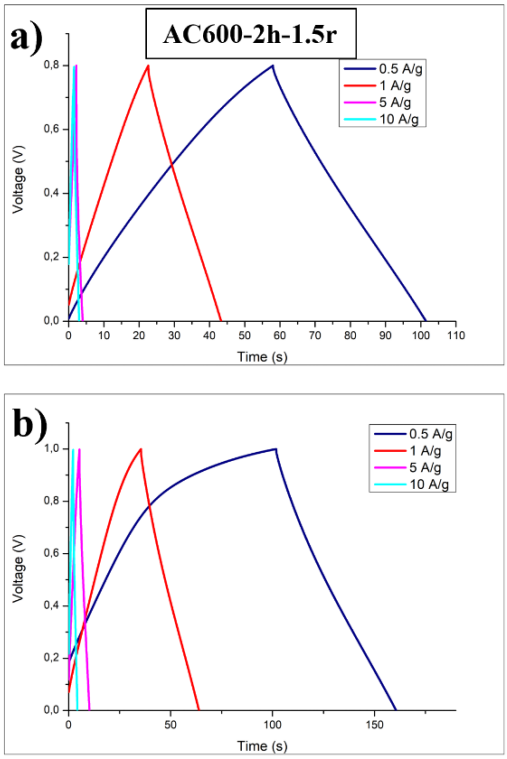

Figure 37. GCD curves of AC600-2h-1.5r for a)0-0.8V and b)0-1.0V

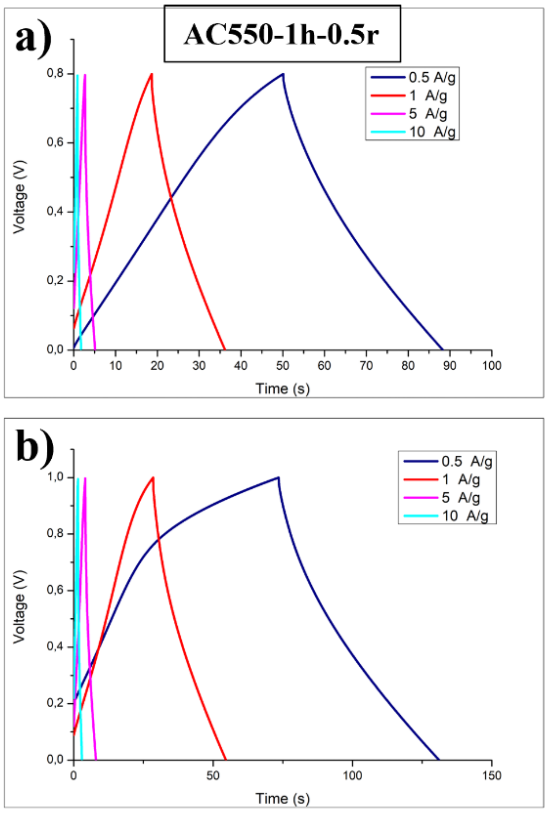

Figure 38. GCD curves of AC550-1h-0.5r for a)0-0.8V and b)0-1.0V

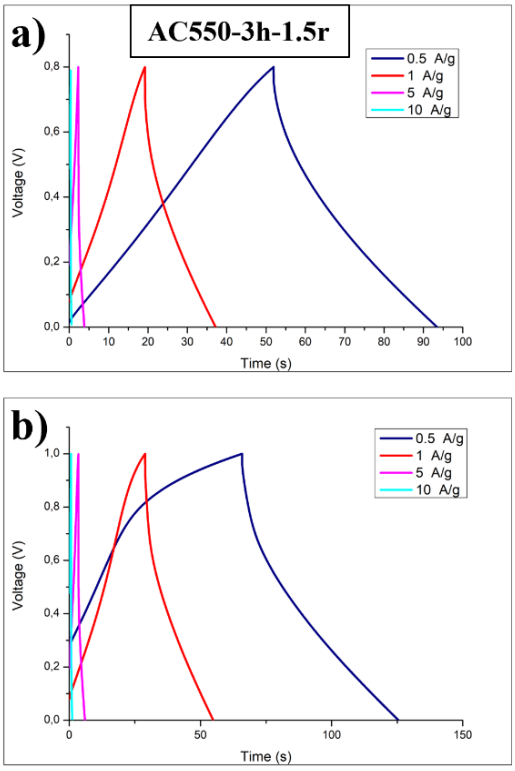

Figure 39. GCD curves of AC550-3h-1.5r for a)0-0.8V and b)0-1.0V

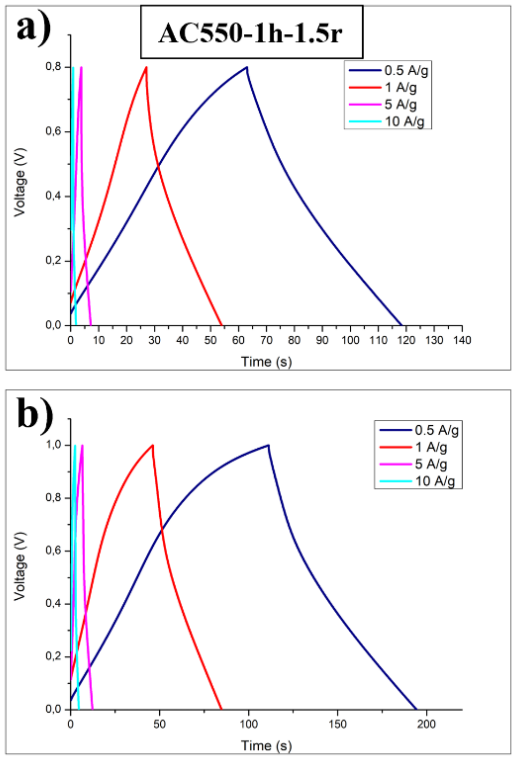

Figure 40. GCD curves of AC550-1h-1.5r for a)0-0.8V and b)0-1.0V

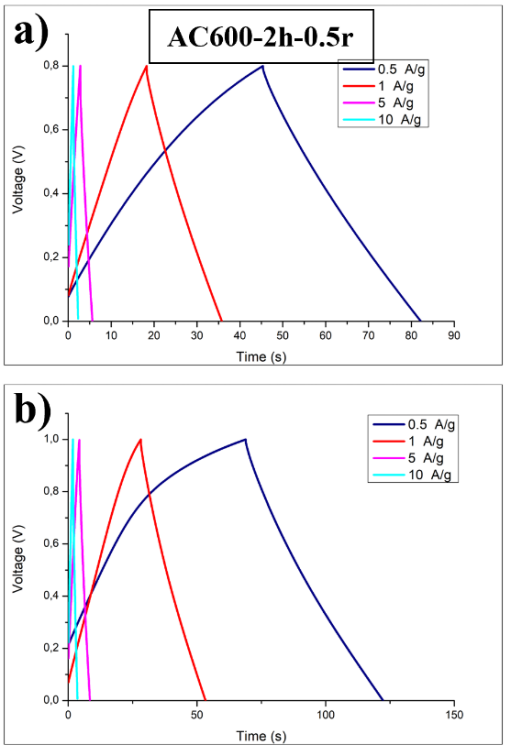

Figure 41. GCD curves of AC600-2h-0.5r for a)0-0.8V and b)0-1.0V

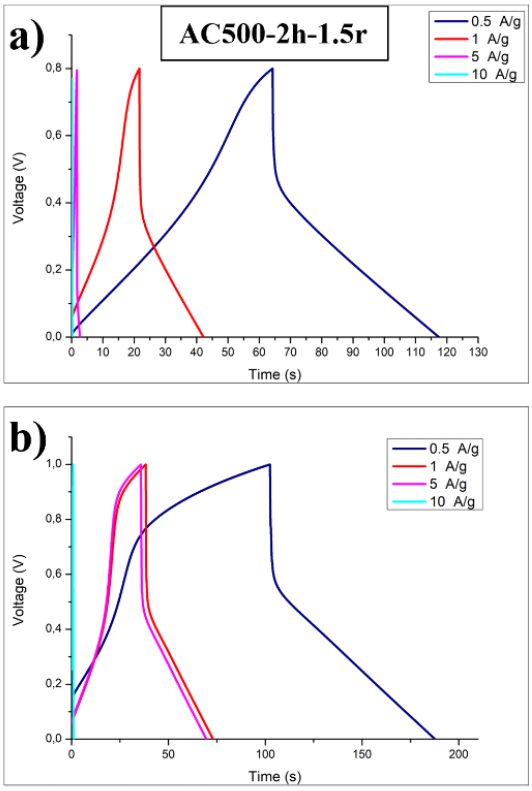

Figure 42. GCD curves of AC500-2h-1.5r for a)0-0.8V and b)0-1.0V

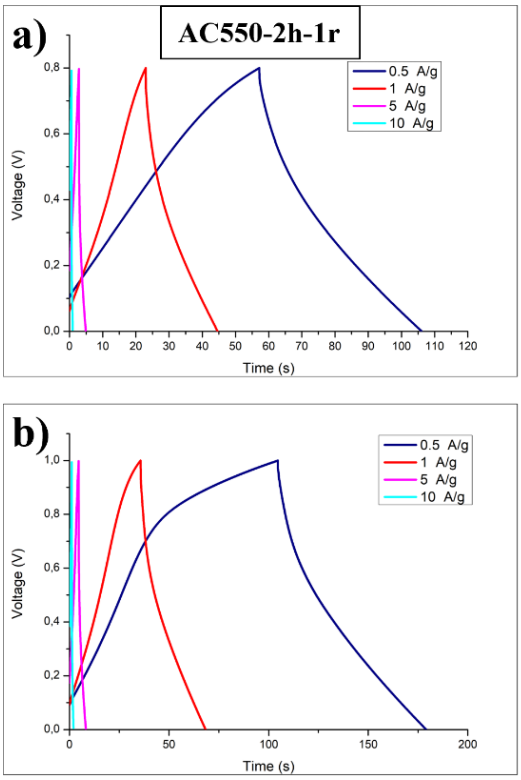

Figure 43. GCD curves of AC550-2h-1r for a)0-0.8V and b)0-1.0V